

Single phage proteins sequester signals from TIR and cGAS-like enzymes

<https://doi.org/10.1038/s41586-024-08122-4>

Received: 8 November 2023

Accepted: 26 September 2024

Published online: 30 October 2024

 Check for updates

Dong Li^{1,7}, Yu Xiao^{2,3,7}, Iana Fedorova^{4,7}, Weijia Xiong^{1,7}, Yu Wang^{1,7}, Xi Liu^{1,7}, Erin Huiting⁴, Jie Ren⁵, Zirui Gao¹, Xingyu Zhao¹, Xueli Cao¹, Yi Zhang¹, Joseph Bondy-Denomy^{4,6} & Yue Feng¹ 

Prokaryotic anti-phage immune systems use TIR and cGAS-like enzymes to produce 1''-3'-glycrocyclic ADP-ribose (1''-3'-gcADPR) and cyclic dinucleotide (CDN) and cyclic trinucleotide (CTN) signalling molecules, respectively, which limit phage replication^{1–3}. However, how phages neutralize these distinct and common systems is largely unclear. Here we show that the Thoeris anti-defence proteins Tad1⁴ and Tad2⁵ both achieve anti-cyclic-oligonucleotide-based anti-phage signalling system (anti-CBASS) activity by simultaneously sequestering CBASS cyclic oligonucleotides. Apart from binding to the Thoeris signals 1''-3'-gcADPR and 1''-2'-gcADPR, Tad1 also binds to numerous CBASS CDNs and CTNs with high affinity, inhibiting CBASS systems that use these molecules *in vivo* and *in vitro*. The hexameric Tad1 has six binding sites for CDNs or gcADPR, which are independent of the two high-affinity binding sites for CTNs. Tad2 forms a tetramer that also sequesters various CDNs in addition to gcADPR molecules, using distinct binding sites to simultaneously bind to these signals. Thus, Tad1 and Tad2 are both two-pronged inhibitors that, alongside anti-CBASS protein 2 (Acb2^{6–8}), establish a paradigm of phage proteins that use distinct binding sites to flexibly sequester a considerable breadth of cyclic nucleotides.

Bacteria encode numerous immune systems that protect them from phage infection^{9–14}. In turn, phages have mechanisms to antagonize these immune systems and effectively replicate, such as expressing proteins with anti-immune activities, among which anti-CRISPR (Acr) proteins have been studied extensively^{15–18}. Thus far, phage anti-immune proteins have been identified for many different systems, including CRISPR–Cas, restriction modification and bacteriophage exclusion, which largely rely on protein–protein interactions to block immune function¹⁹. However, recently identified inhibitors of cyclic nucleotide signalling-based anti-phage systems, such as CBASS, Thoeris, Pyscar and type III CRISPR–Cas, have revealed the ability of phage proteins to sequester or degrade cyclic nucleotides^{4–7,20,21}.

The Thoeris anti-phage system encodes ThsB, a protein with a Toll/interleukin-1 receptor/resistance (TIR) domain that senses phage infection and produces the 1''-3' gcADPR that subsequently activates the NADase effector ThsA^{1,2,4}. CBASS encodes a cyclic GMP-AMP synthase (cGAS)/DncV-like nucleotidyltransferase (CD-NTase) that produces CDNs or CTNs after phage infection³. A broad diversity of CD-NTases has been identified in bacteria²², which are able to produce at least 12 different cyclic oligonucleotide species^{22–27}. These cyclic nucleotides bind to a cognate effector, which is proposed to induce dormancy or death to stop successful phage replication.

The Thoeris anti-defence proteins Tad1 and Tad2 antagonize immunity by sequestering the signalling molecule 1''-3'-gcADPR^{4,5}. For CBASS,

two phage proteins have been identified that antagonize its immunity. Anti-CBASS protein 1 (Acb1) degrades the cyclic oligonucleotide signals²⁰, and Acb2 is a sponge for CDNs^{6,7} and CTNs with two distinct binding sites⁸. Here we report that Tad1 and Tad2 both also possess anti-CBASS activity by sequestering a breadth of CBASS signals, each using two distinct binding pockets. CBASS is generally more common than Thoeris²⁸; thus, these findings greatly broaden our appreciation of the utility of these proteins to the many phages that encode them. Some bacterial species also encode both Thoeris and CBASS immune systems^{14,29}, which Tad1 and Tad2 could inhibit simultaneously. Tad1 and Tad2 are therefore two-pronged inhibitors that block Thoeris and CBASS activity due to the similar nature of their immune signalling molecules despite the independent evolutionary origins of the enzymes that create them.

Tad1 sequesters CBASS CTNs and CDNs

Owing to the overall similarities between signalling molecules used by multiple defence systems, we examined whether anti-Thoeris Tad1 and Tad2 sponges also sequester cyclic nucleotides used in Pyscar, CBASS or type III CRISPR–Cas signalling systems^{30–32}. Four cyclic mononucleotides (cCMP, cUMP, cGMP and cAMP), eight CDNs (3',3'-cGAMP, cGG, cUG, cUA, cUU, cAA, 2',3'-cGAMP and 3',2'-cGAMP), two CTNs (cA₃ and cAAG), as well as cA₄ and cA₆ were tested. Native gel assays showed a

¹State Key Laboratory of Chemical Resource Engineering, Beijing Advanced Innovation Center for Soft Matter Science and Engineering, College of Life Science and Technology, Beijing University of Chemical Technology, Beijing, China. ²State Key Laboratory of Plant Diversity and Specialty Crops, Institute of Botany, Chinese Academy of Sciences, Beijing, China. ³Beijing Advanced Innovation Center for Structural Biology, Beijing Frontier Research Center for Biological Structure, School of Life Sciences, Tsinghua University, Beijing, China. ⁴Department of Microbiology and Immunology, University of California, San Francisco, San Francisco, CA, USA. ⁵State Key Laboratory for Biology of Plant Diseases and Insect Pests, Ministry of Agriculture, Institute of Plant Protection, Chinese Academy of Agricultural Sciences, Beijing, China. ⁶Quantitative Biosciences Institute, University of California, San Francisco, San Francisco, CA, USA. ⁷These authors contributed equally: Dong Li, Yu Xiao, Iana Fedorova, Weijia Xiong, Yu Wang, Xi Liu.  e-mail: Joseph.Bondy-Denomy@ucsf.edu; fengyue@mail.buct.edu.cn

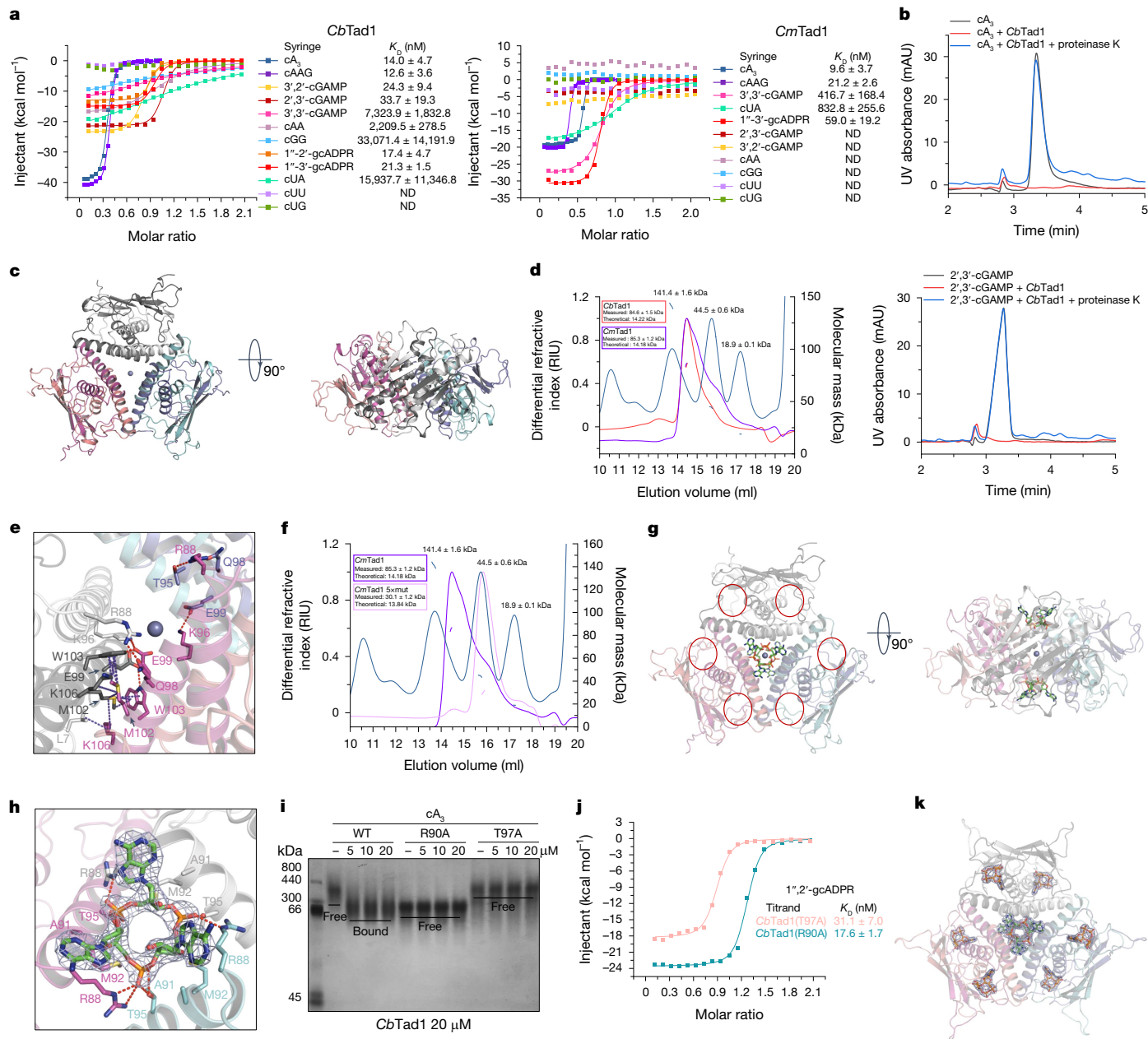


Fig. 1 | The Tad1 hexamer binds to two molecules of cyclic trinucleotides.

a, ITC assay of cyclic oligonucleotide binding to *CbTad1* and *CmTad1*. Representative binding curves and binding affinities are shown. The K_D values are mean ± s.d. $n = 3$ independent experiments. Raw data are shown in Supplementary Fig. 3. **b**, The ability of *CbTad1* to bind to and release cA₃ and 2',3'-cGAMP when treated with proteinase K was analysed using HPLC. **c**, The overall structure of *CmTad1* hexamer. The Zn ion is shown as a sphere. Three views are shown. **d**, SLS assays of *CbTad1* and *CmTad1*. Theoretical and measured values are shown. The chromatogram shows the elution profile of protein standards. **e**, Detailed binding in the hexamer interface of *CmTad1*. Residues involved in hexamer formation are shown as sticks. The red dashed lines represent polar interactions. **f**, SLS assays of *CmTad1* and its mutant. 5× mut, *CmTad1*(Q98A/E99A/M102A/W103A/K106A). **g**, The overall structure of the

CmTad1 hexamer bound to cA₃. Two views are shown. The red circles mark the binding sites of gcADPR. **h**, Detailed binding between *CmTad1* and cA₃. Residues involved in cA₃ binding are shown as sticks. The red dashed lines represent polar interactions. 2Fo-Fc electron density of cA₃ within one binding pocket is shown and contoured at 1 σ . **i**, Native-PAGE analysis showing the binding of *CbTad1* and its mutants to cA₃ and 1'',2'-gcADPR. Gel source data are provided in Supplementary Fig. 1. **j**, ITC assays of the binding of 1'',2'-gcADPR to *CbTad1* mutants. The K_D values are mean ± s.d. $n = 3$ independent experiments. Raw data are shown in Supplementary Fig. 3. **k**, The overall structure of the *CmTad1* hexamer bound to cA₃ and 1'',3'-gcADPR. cA₃ and 1'',3'-gcADPR are shown as green and orange sticks, respectively. 2Fo-Fc electron density of cA₃ and 1'',3'-gcADPR within the *CbTad1* hexamer contoured at 1 σ .

shift in Tad1 from both *Clostridium botulinum* prophage (*CbTad1*) and *Clostridioides mangenotii* prophage (*CmTad1*) after the addition of cA₃ or cAAG, and a shift in *CbTad1* after the addition of 2',3'-cGAMP or 3',2'-cGAMP (Supplementary Figs. 1 and 2). These binding events were further verified by isothermal calorimetry (ITC) experiments (Fig. 1a and Supplementary Fig. 3), which showed that *CbTad1* and *CmTad1* bind to cA₃ with a K_D of around 14.0 nM and 9.8 nM, respectively, and

they bind to cAAG with a K_D of about 12.5 nM and 20.1 nM, respectively (Fig. 1a). *CbTad1* bound to 2',3'-cGAMP and 3',2'-cGAMP with a K_D of around 31.1 nM and 24.5 nM, respectively (Fig. 1a and Supplementary Fig. 3); however, it bound only weakly ($K_D > 0.4 \mu\text{M}$) to 3',3'-cGAMP, cGG, cUA and cAA (Fig. 1a and Supplementary Fig. 3). An analysis using high-performance liquid chromatography (HPLC) revealed that incubating *CbTad1* with cA₃ or 2',3'-cGAMP depleted detectable molecules,

but they were detected again in unmodified form after proteolysis of *CbTad1* (Fig. 1b). The strong binding values reported here are more than one order of magnitude stronger than the reported *CmTad1* binding affinity for 1''-2'-gcADPR of 241 nM (ref. 4), which was the first identified ligand for this protein. Bioinformatic analysis of the *Clostridium* genus revealed CBASS CD-NTases that produce cA₃/cAAG (CdnD) and 3',2'-cGAMP (CdnG)^{22,23} (Extended Data Fig. 1a and Supplementary Table 1), highlighting the likely biological driver for the observed binding spectra of *CbTad1* and *CmTad1*. Taken together, these results demonstrate that Tad1 also binds to and sequesters both CTNs and CDNs used in CBASS immunity in addition to Thoeris gcADPR molecules.

Tad1 hexamer binds to CTNs and gcADPR differently

To understand how Tad1 interacts with CTNs, we first determined crystal structures of apo *CmTad1* (2.56 Å) and its complex with cA₃ (2.80 Å) or cAAG (3.27 Å) (Extended Data Table 1). Notably, in all of the structures solved, *CmTad1* is a hexamer (Fig. 1c), rather than a dimer as previously proposed for *CbTad1*⁴. To verify the oligomeric state of Tad1 in solution, we performed static light scattering (SLS) analysis of *CmTad1* and *CbTad1*, which also showed that both are hexamers in solution (Fig. 1d). The Tad1 hexamer can be viewed as a trimer of dimers with dihedral *D*₃ symmetry (Fig. 1c), and analysis of the interface between two dimers showed that each protomer interacts with protomers from the other two dimers (Fig. 1e). By mutating the interface residues of *CbTad1* and *CmTad1*, the protein peaks of the mutants shifted in the gel-filtration assay, and SLS analysis showed that both mutant proteins were dimers (Fig. 1f and Extended Data Fig. 2e).

We next investigated the binding pockets of the CTNs. We found that a Tad1 hexamer binds to two CTNs in distinct pockets separate from gcADPR-binding sites. CTNs are bound in the trimeric interface of the three Tad1 dimers (Fig. 1g and Supplementary Fig. 4c), coordinated by conserved residues Arg88 and Thr95 in *CmTad1* (Fig. 1h). Mutations R90A and T97A in *CbTad1* reduced cA₃ binding but not gcADPR binding (Fig. 1i,j), confirming independent binding sites for CTNs and gcADPR. An analysis of the structure of Tad1 is provided in the Supplementary Information. Thus, one Tad1 hexamer binds to two CTNs through two pockets independent of those for gcADPR, which was confirmed by solving a structure of *CmTad1* in a complex with cA₃ and 1''-3'-gcADPR (Fig. 1k).

Tad1 binds to CDNs and gcADPR in the same pocket

To understand how Tad1 interacts with CDNs, we determined crystal structures of *CbTad1* in a complex with 2',3'-cGAMP at 2.37 Å (Extended Data Fig. 3a and Extended Data Table 1). Notably, 2',3'-cGAMP binds in the same binding pocket as gcADPR in *CbTad1* (Extended Data Figs. 3b and 4a,b) and a *CbTad1* hexamer therefore binds to six 2',3'-cGAMP molecules in total with two in each *CbTad1* dimer (Extended Data Fig. 3a). A detailed structural analysis and the structural basis of CDN specificity are provided in Extended Data Fig. 4c,d and Supplementary Information.

Tad1 homologues differ in CDN binding spectra

The different binding spectra of CDNs between *CbTad1* and *CmTad1* suggested that other Tad1 homologues might show diverse CDN binding spectra. Generation of a phylogenetic tree using PSI-BLAST to identify Tad1 homologues revealed numerous distinct clades of Tad1 and showed that *CbTad1* and *CmTad1* are represented on distant branches of the Tad1 phylogenetic tree (Supplementary Fig. 7). Importantly, most Tad1 orthologues are expected to retain both CDN/gcADPR- and CTN-binding sites, whereas only 12% and 6% of proteins have substitutions in CDN/gcADPR- or CTN-binding sites, respectively (Supplementary Fig. 7). To test the binding activities of diverse homologues, we

purified Tad1 from *Bacillus cereus* phage SBSPhiJ7 (called SBS Tad1 here) and *Colidextribacter* sp. OB.20 (called ColiTad1 here) and determined their binding to the same array of cyclic oligonucleotides by native gel (Supplementary Fig. 8) combined with ITC assays (Supplementary Fig. 9). Both SBS Tad1 and ColiTad1 also bind to cA₃/cAAG and cADPR isomers, demonstrating a broadly conserved function of this family. Notably, SBS Tad1 binds to 3',3'-cGAMP/cUA with a high affinity (K_D values of 48.7 nM and 53.9 nM, respectively) and 2',3'-/3',2'-cGAMP with a low affinity (Fig. 2a and Supplementary Figs. 8 and 9), which is the opposite of *CbTad1*. These K_D values are also strong compared with the SBS Tad1 binding affinity for 1''-2'- and 1''-3'-gcADPR of 284 nM and 210 nM, respectively (Fig. 2a and Supplementary Fig. 9). Moreover, ColiTad1 binds to 2',3'-cGAMP with a high affinity and 3',3'-/3',2'-cGAMP with a low affinity. Analysis of the well-sequenced *B. cereus* group, the bacterial hosts for SBS Tad1, revealed multiple commonly encoded CBASS CD-NTases (that is, CdnB, CdnD, CdnE and CdnG) that produce the spectrum of cyclic oligonucleotides that SBS Tad1 binds to (Extended Data Fig. 1d). This observation puts forth a clear biological need to inhibit diverse CBASS systems. None of the known CD-NTases used in our search were identified in *Colidextribacter* genomes. Taken together, these results indicate that Tad1 homologues maintain a conserved ability to bind to CBASS CTN and gcADPR signals, with a variable spectrum of high-affinity binding to CBASS CDNs (Fig. 2b).

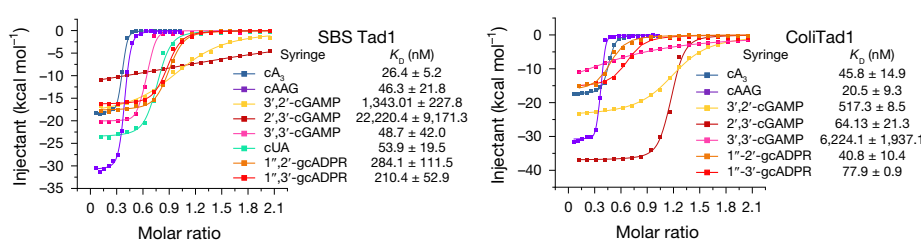
Tad1 antagonizes two CBASS systems

As SBS Tad1 displays high-affinity binding to 3',3'-cGAMP, we tested whether SBS Tad1 can inhibit type II-A^{GA} CBASS immunity that uses 3',3'-cGAMP to activate a phospholipase (CapV) effector protein. To this end, we first used an *in vitro* CapV activity assay we set up previously⁶. While CapV activity could be activated by 3',3'-cGAMP, its activity was abolished when SBS Tad1 was preincubated with 3',3'-cGAMP (Fig. 2c). After proteolysis of SBS Tad1, the released molecule again activated the CapV activity. The SBS Tad1 mutants F100A/N110A and R127A/R131A, designed on the basis of its conserved CDN-binding sites, both displayed decreased 3',3'-cGAMP binding (Supplementary Fig. 10) and reduced inhibition of CapV activity (Fig. 2c). Compared with SBS Tad1, other Tad1 homologues did not show significant inhibition of CapV activity, probably due to their weak binding to 3',3'-cGAMP (Fig. 2d). These results demonstrate that SBS Tad1 antagonizes type II-A^{GA} CBASS immunity *in vitro* through sequestering 3',3'-cGAMP. To determine whether SBS Tad1 can inhibit this same 3',3'-cGAMP-based CBASS system *in vivo*, the different Tad1 proteins were expressed in the *Pseudomonas aeruginosa* strain BWHPSA011 (Pa011) with an active type II-A^{GA} CBASS system⁶. The Tad1 homologs were also expressed in a strain that expresses a Thoeris operon (PAO1:Tn7 Thoeris SIR2), to confirm expression and function of Tad1 proteins in this host. We performed phage infection assays with the CBASS-targeted phage PaMx41 that lacks the anti-CBASS gene acb2 (PaMx41(Δacb2)) or the Thoeris-targeted phage F10. We observed that SBS Tad1, but not *CmTad1* or *CbTad1*, inhibited type II-A^{GA} CBASS activity to nearly the same extent as the Acb2 positive control, while all Tad1 proteins blocked Thoeris function (Fig. 2e). These data collectively demonstrate the SBS Tad1 homologue inhibiting a 3',3'-cGAMP CBASS system *in vivo*, consistent with *in vitro* binding patterns.

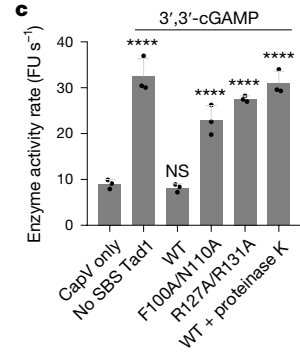
As all of the Tad1 homologues tested display high-affinity binding to CTNs, we tested whether Tad1 can inhibit type III-C^{AAA} CBASS immunity that uses cA₃ to activate a non-specific endonuclease (NucC) effector protein^{33,34}. Using the NucC enzyme from *P. aeruginosa* strain ATCC 27853 (Pa278), we showed that addition of cA₃ activates the DNA cleavage activity, whereas adding *CbTad1* significantly decreased NucC activity (Fig. 2f). Moreover, after proteolysis of *CbTad1*, the released cA₃ molecule again activated the NucC activity (Fig. 2f). The R90A and T97A *CbTad1* mutant proteins, with diminished cA₃ binding, displayed no inhibition of NucC activity. To test *in vivo* activity, the same Pa278

Article

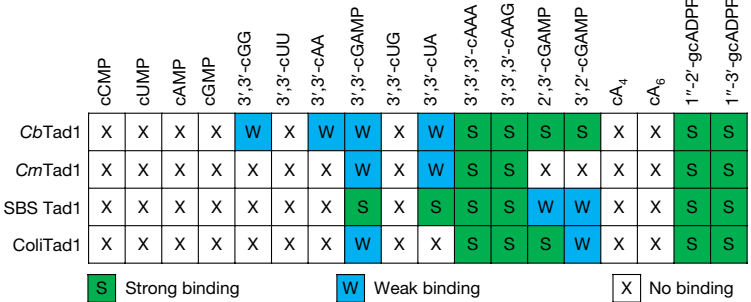
a



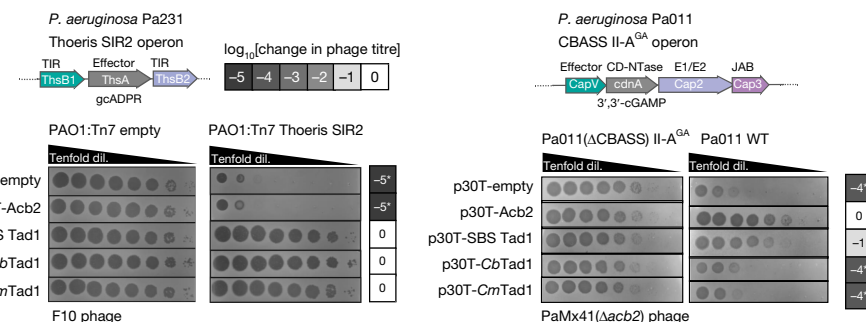
c



b



e



g



h

log₁₀[change in phage titre]

-5 -4 -3 -2 -1 0

i

log₁₀[change in phage titre]

-5 -4 -3 -2 -1 0

Fig. 2 | Tad1 antagonizes type II-A^{GA} and type III-C^{AAA} CBASS immunity.

a, ITC analysis of cyclic oligonucleotides binding to SBS Tad1 and ColiTad1. Representative binding curves and binding affinities are shown. The K_D values are mean ± s.d. $n = 3$ independent experiments. Raw data for these curves are shown in Supplementary Fig. 3. **b**, Summary of Tad1-binding results. X, no binding; W, weak, $K_D > 400$ nM. S, strong, $K_D < 400$ nM. **c**, CapV enzyme activity in the presence of 3',3'-cGAMP and resorufin butyrate. The enzyme activity rate was measured by the accumulation rate of fluorescence units (FU) per second. Data are mean ± s.d. $n = 3$ independent experiments. **d**, CapV enzyme activity with Tad1 homologues. The experiment was performed as in **c**. For **c** and **d**, statistical analysis was performed using GraphPad Prism using the in-built one-way analysis of variance ANOVA with Dunnett's multiple-comparison test versus CapV only. **e**, Phage plaque assays

with F10 phage spotted in tenfold serial dilutions (dil.) against Thoeris or PaMx41(Δacb2) against type II-A^{GA} CBASS, with p30T plasmid expressing Tad1 genes. The asterisks indicate the presence of faint phage plaques. **f**, Agarose gel showing cAAA activation of NucC nuclease on DNA. L, linear; N, nicked plasmid; SC, supercoiled plasmid. Linear and cut denote digested DNA. **g**, Plaque assays with JBD67(Δacb2) phage spotted in tenfold serial dilutions onto a lawn of *P. aeruginosa* cells with or without the Pa278 CBASS operon. **h**, Plaque assays with WT JBD67 phage, JBD67(Δacb2) or JBD67 SBS Tad1 (introduction of *SBS tad1* gene in place of the *acb2* gene in JBD67 genome), plated as in **g**. **i**, Plaque assays with phiKZ or phiKZ(Δorf184) phage spotted in tenfold serial dilutions onto lawns of *P. aeruginosa* cells expressing the indicated defence system. For **e–i**, three replicates were performed for each experiment and the results were similar each time. **** $P < 0.0001$; NS, not significant.

type III-C^{AAA} CBASS operon was chromosomally integrated into strain PAO1 (PAO1:Tn7 CBASS III-C). Pa278 CBASS reduced the titre of phage JBD67($\Delta acb2$) by three orders of magnitude (Fig. 2g). Co-expression of SBS Tad1, CbTad1, CmTad1 or an Acb2 control all fully inhibited cA₃-based CBASS activity and rescued JBD67($\Delta acb2$) phage titre. Introduction of R127A/R131A mutations in SBS Tad1, which disrupt 1''-3'-gcADPR and 3',3'-cGAMP binding, led to the loss of anti-Thoeris and anti-CBASS II-A^{GA} activity, while the R108A mutation, which disrupts cAAAE binding, abolished anti-CBASS III-C^{AAA} activity in vivo (Extended Data Fig. 5). Moreover, introduction of the SBS *tad1* gene into the genome of phage JBD67 in place of the endogenous *acb2* gene functionally replaced *acb2*, enabling the phage to replicate on the type III-C^{AAA} host (Fig. 2h).

To determine whether phages encoding Tad1 are naturally resistant to CBASS, we used BLASTp to search for Tad1 homologues in *P. aeruginosa* phages. We identified a Tad1 homologue encoded by the jumbo phage phiKZ, encoded by *orf184* (Extended Data Fig. 6a). This gene is predicted to encode a protein that has a Tad1 domain in addition to a domain that probably enables packaging of the protein into the phiKZ virion (Extended Data Fig. 6b). phiKZ gp184 is proteolysed before the His109 position³⁵ and the proteolysed gp184, with just the Tad1 domain remaining, is packaged into the phage virion and delivered into the cell during infection³⁶. To examine its role in immune evasion, we used a previously established method³⁷ to delete *orf184*. While wild-type (WT) phiKZ is resistant to type II-A^{GA}, the $\Delta orf184$ mutant phage was fully targeted by type II-A^{GA} CBASS, demonstrating a natural anti-CBASS role (Fig. 2i). However, the mutant phage still resisted III-C^{AAA} CBASS. Notably, gp184 in vitro bound tightly to 3',3'-cGAMP but poorly to cA₃ (Extended Data Fig. 6c,d). Indeed, the CTN-binding site for gp184 is mutated (Glu195 and Asn202 residues) and is probably unable to support binding (Extended Data Fig. 6a), suggesting that phiKZ resists type III-C^{AAA} CBASS for another reason. WT phiKZ was partially targeted by type I Thoeris while the phiKZ $\Delta orf184$ mutant was completely targeted in the presence of Thoeris (Fig. 2i). Expression of the Tad1 domain of gp184 complemented the phiKZ($\Delta orf184$) titre on a CBASS II-A^{GA} lawn and partially restored the titer on a type I Thoeris lawn (Extended Data Fig. 6e). Consistent with these data, phiKZ gp184 binds only weakly to gcADPR in vitro, explaining why the WT phage is partially targeted (Extended Data Fig. 6c,d). Together, these data provide in vivo and in vitro evidence that Tad1 is a flexible anti-CBASS sponge protein, binding to both CDNs and CTNs involved in immunity, as well as an effective anti-Thoeris sponge protein.

HgmTad2 sequesters multiple CBASS CDNs

Tad2 is a recently identified anti-Thoeris sponge encoded by *B. cereus* phage SPO1 that works by sequestering gcADPR through a structural fold completely different from Tad1⁵. Using the same array of cyclic nucleotides that we used to study Tad1, we first tested SPO1 Tad2 binding. While binding to gcADPR molecules was confirmed by native gel (Extended Data Fig. 7a), no substantial shift in SPO1 Tad2 was observed after the addition of any of the other cyclic nucleotides (Extended Data Fig. 7a), suggesting that SPO1 Tad2 might not bind to any of these signalling molecules.

The Tad2 family of proteins is quite widespread in numerous mobile genetic elements, with a previously annotated domain of unknown function DUF2829. We therefore selected a diverged homologue (called HgmTad2 here), derived from human gut metagenomic libraries³⁸. We decided to test whether HgmTad2 also sequesters gcADPR molecules. Notably, during purification, HgmTad2 eluted in three separate peaks in the process of ion-exchange chromatography (Extended Data Fig. 8a), which displayed different migrations through a native gel. We collected the three components separately and tested whether they bind to gcADPR molecules. A native gel assay showed a shift in the purified HgmTad2 protein in all of the three states after the addition of 1''-2'-gcADPR (Extended Data Fig. 8b), suggesting gcADPR binding.

We next solved the structures of HgmTad2 and the HgmTad2-1''-2'-gcADPR and HgmTad2-1''-3'-gcADPR complexes (Extended Data Table 1). Purified HgmTad2 in the three different states was used separately during crystallization. Notably, during structure solution, we found that a clear density with a shape similar to that of 3',3'-cyclic di-GMP (cGG) was visible in all of the solved structures using HgmTad2 of states 2 and 3 (Fig. 3a), which simultaneously contained gcADPR molecules at a distinct site when co-expressed with gcADPR-producing enzymes. However, there was no such cGG-like density in the structures using HgmTad2 in state 1. This suggested that HgmTad2 in states 2 and 3 contains cGG or another similar molecule bound during its expression in *Escherichia coli*. To verify that the density corresponds to cGG, purified HgmTad2 in states 2 and 3 was denatured by heating and filtered to obtain the nucleotide within the protein. The filtered nucleotide showed a similar retention time to cGG, but markedly different from that of 3',3'-cGAMP (Fig. 3b), further supporting that the nucleotide within purified HgmTad2 in states 2 and 3 is cGG. However, the sample of HgmTad2 in state 1 after the same procedure showed no peak here (Fig. 3b). Together, these findings show that HgmTad2 can bind to cGG and gcADPR simultaneously, and a large fraction of the purified HgmTad2 contains bound cGG from expression in *E. coli*.

Binding of cGG by HgmTad2 was unexpected, and this inspired us to consider that HgmTad2 might also bind to other CDNs. To exclude the influence of bound cGG within HgmTad2 in binding assays, we collected only HgmTad2 in state 1 to test its binding spectrum using native gel assays, which showed a substantial shift in HgmTad2 after the addition of 3',2'-cGAMP, 3',3'-cGAMP, cGG and cUG, and a minor shift after the addition of 2',3'-cGAMP, but no shift after the addition of CTNs or other nucleotides (Fig. 3c). These binding events were further verified by surface plasmon resonance (SPR) experiments, which showed that HgmTad2 binds to 3',2'-cGAMP, 3',3'-cGAMP, 2',3'-cGAMP and cUG with a K_D of around 0.51, 0.83, 670 and 1.01 nM, respectively (Fig. 3d and Extended Data Fig. 8c). Notably, the binding K_D of cGG to HgmTad2 was calculated as high as 24.2 pM, possibly explaining why HgmTad2 stably bound to endogenous cGG during its expression in *E. coli*. HPLC assays demonstrated that HgmTad2 depletes 3',3'-cGAMP, but does not degrade it (Fig. 3e), while SPO1 Tad2 does not deplete the molecule (Extended Data Fig. 7b,c). Taken together, these results demonstrate that HgmTad2 sequesters cGG and multiple CDNs used in CBASS immunity, in addition to gcADPR molecules.

Tad2 binds to CDNs and gcADPR differently

We next show the structures of HgmTad2 alone and in complex with gcADPR and CDNs. We solved a total of six structures of HgmTad2 and compared them with the structure of SPO1 Tad2⁵. HgmTad2 forms a tetramer similarly to SPO1 Tad2 (Fig. 3f,g), and the tetrameric state of HgmTad2 and SPO1 Tad2 were also verified by SLS analysis (Supplementary Fig. 12a). Both SPO1 Tad2 and HgmTad2 tetramer bind to two gcADPR molecules with two identical binding pockets, which are located in the middle region of the tetramer at the interface of two protomers from different dimeric units (Fig. 4a). Specifically, the binding between 1''-2'-gcADPR and HgmTad2 involves hydrogen bonds and hydrophobic interactions with specific residues, mutations of which significantly reduce gcADPR binding and the inhibition of ThsA NADase activity by HgmTad2 (Fig. 4b,c and Extended Data Fig. 9c).

Structural analysis subsequently revealed that HgmTad2 additionally binds to CDNs 3',3'-cGAMP, cGG, cUG and 3',2'-cGAMP in a region of the protein distinct from that of 1''-2'-gcADPR (Fig. 4d), with the CDNs all binding to the same pocket (for example, cGG and 3',3'-cGAMP, compared in Extended Data Fig. 9d,e). In the HgmTad2-cGG complex, ligand binding is mediated by extensive hydrophobic and polar interactions. To verify these residues, we mutated interacting residues of HgmTad2 (S47A, F70A and R31A/N85A) and tested their binding to both cGG and 3',3'-cGAMP. Consistently, native gel analysis showed no

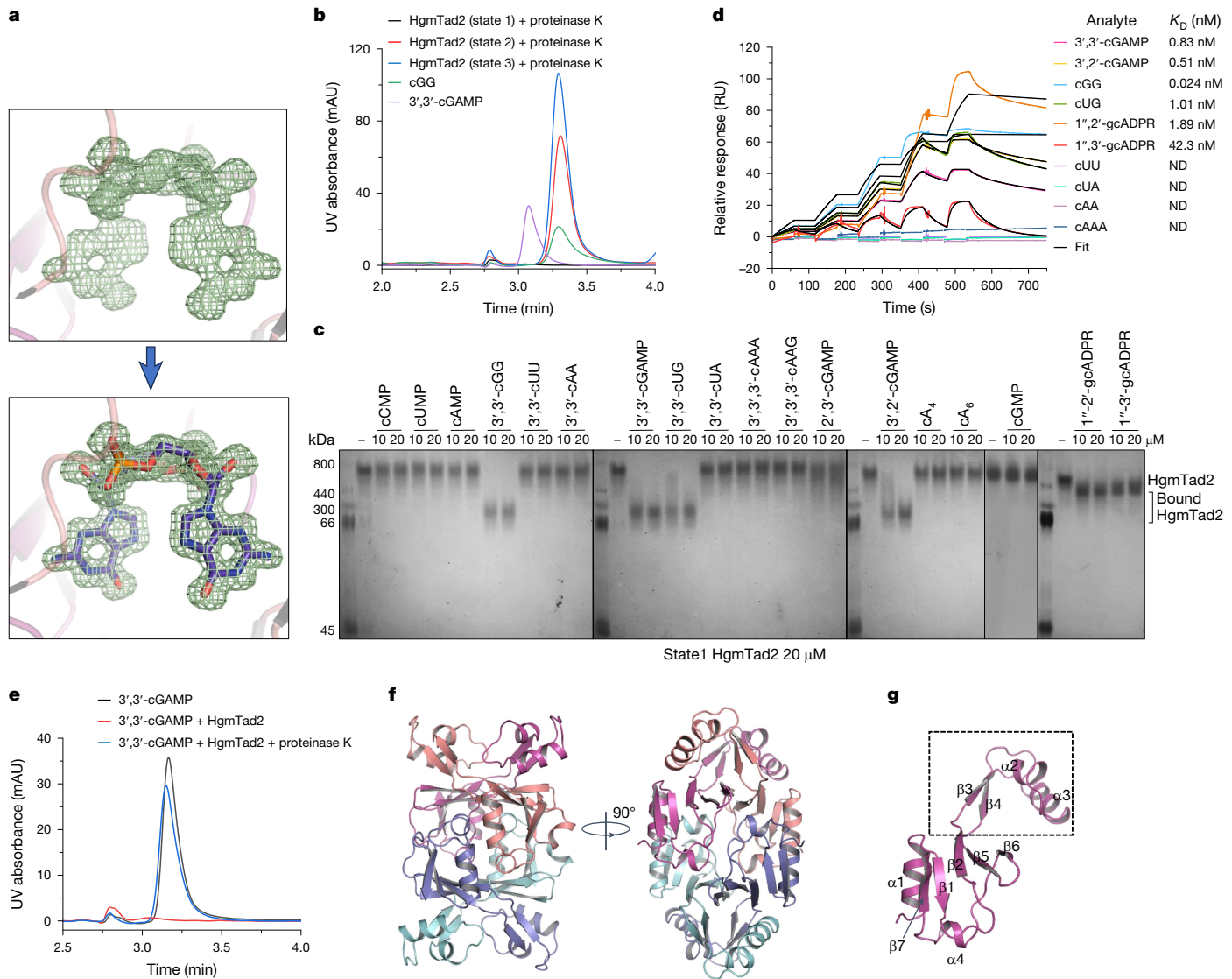


Fig. 3 | Tad2 binds to an array of CDNs. **a**, The Fo-Fc density around the putative cGG in the structure of state 3 HgmTad2 contoured at 2.5σ . The density itself and with cGG placed are shown at the top and bottom, respectively. **b**, The molecules in HgmTad2 of three states released when treated with proteinase K was analysed using HPLC. 3',3'-cGAMP and cGG standards were used as controls. **c**, Native-PAGE analysis of the binding of state 1 HgmTad2 to cyclic oligonucleotides and gcADPR molecules. Gel source data are provided in Supplementary Fig. 1. **d**, Overlay of sensograms from SPR experiments used

to determine kinetics of HgmTad2 binding to CDNs. Data were fit with a model describing one-site binding for the ligands (black lines). **e**, The ability of state 1 HgmTad2 to bind and release 3',3'-cGAMP when treated with proteinase K was analysed using HPLC. 3',3'-cGAMP standard was used as a control. The remaining nucleotides after incubation with HgmTad2 were tested. **f**, The overall structure of the HgmTad2 tetramer. Two views are shown. **g**, Structure of a protomer of HgmTad2. Secondary structures are labelled.

shift in these mutants after the addition of either cGG or 3',3'-cGAMP (Fig. 4e,f and Extended Data Fig. 9i). We next confirmed that the binding sites of the cyclic dinucleotides and gcADPR in HgmTad2 are independent of each other. We tested the binding of 1''-2'-gcADPR to S47A, F70A and R31A/N85A mutant proteins, as well as the binding of cGG or 3',3'-cGAMP to W21A/N22A and S90A/T92A/D93A mutant proteins. The results showed that mutation of the binding site for one molecule does not decrease the binding of the other (Fig. 4g). This is also consistent with the fact that we obtained the co-structures of HgmTad2-1''-2'-gcADPR-cGG and HgmTad2-1''-3'-gcADPR-cGG (Fig. 4h-i). Thus, an HgmTad2 tetramer can bind to two cyclic dinucleotides and two gcADPR molecules simultaneously.

HgmTad2 binds to CDNs with its insertion between $\beta 2$ and $\beta 5$; this region is much shorter in SPO1 Tad2 (Fig. 5a). As the binding to cGG results from the insertion between $\beta 2$ and $\beta 5$ of HgmTad2 (Extended Data Fig. 9f), we performed a sequence-based analysis to search for

Tad2 homologues with long insertions like HgmTad2 that may enable binding to CDNs (Fig. 5b and Supplementary Fig. 13). Notably, two of such Tad2 homologues from *Sphingobacterium thalpophilum* (*SptTad2*) and *Salegentibacter* sp. BDJ18 (*SaTad2*) with similarly long insertions also bind to CDNs with different affinities (Fig. 5c–e and Supplementary Fig. 14). *SptTad2* binds to cGG with a high affinity and has a similar cGG-binding pocket to HgmTad2 (Fig. 5f,g), demonstrating that Tad2 homologues can bind to CDNs with their large insertion domain, while the gcADPR-binding site is highly conserved across Tad2 proteins.

Structural analysis of Tad2 binding to other CDNs and gcADPR is shown in the Supplementary Information.

Tad2 blocks two CBASS systems

Diguanylate cyclases produce cGG in many Gram-negative bacteria and are distinct enzymes from the CD-NTases that make CBASS nucleotides.

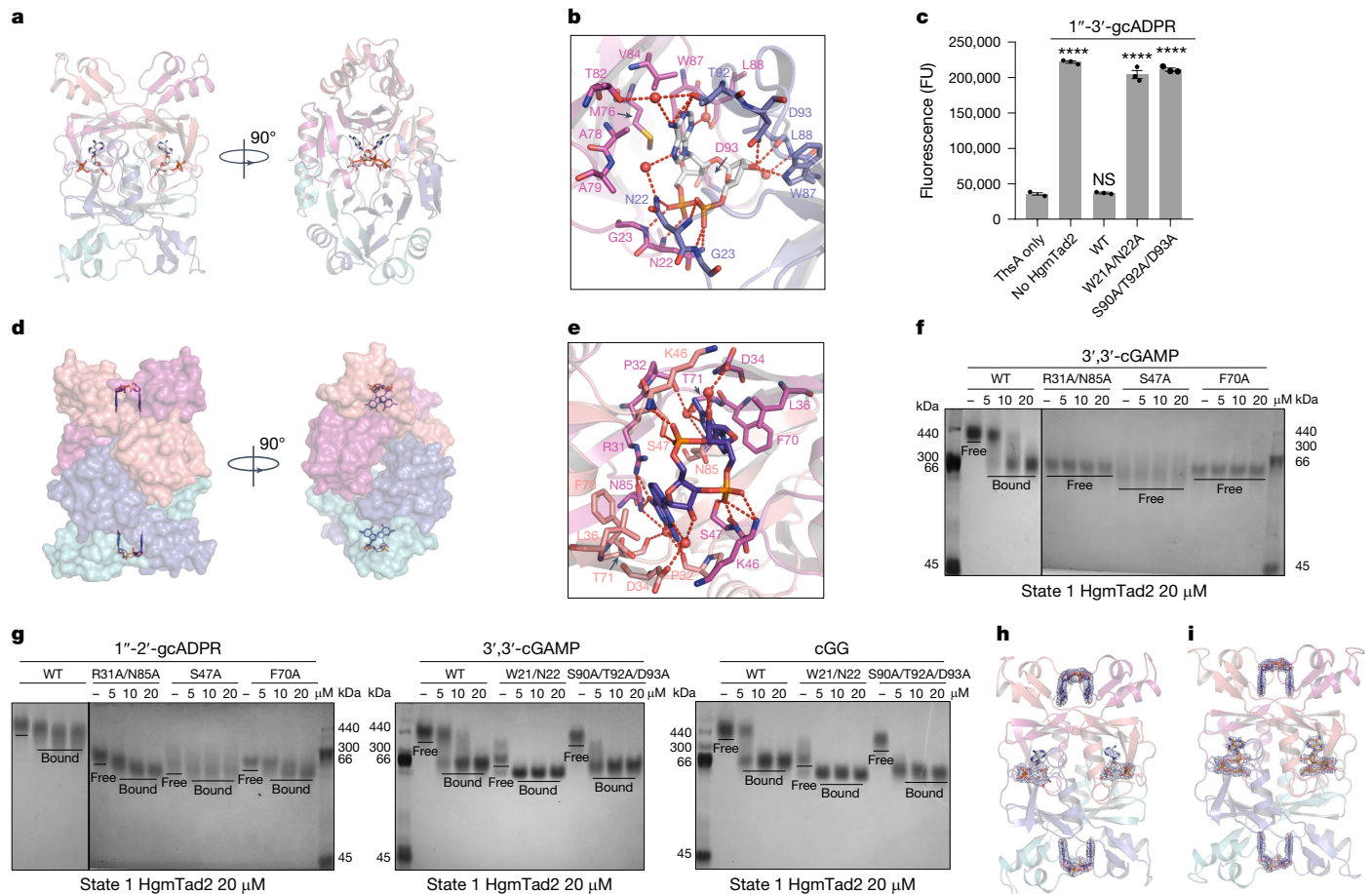


Fig. 4 | Tad2 binds to CDs and gcADPR molecules simultaneously. **a**, The overall structure of HgmTad2 tetramer bound to 1''-2'-gcADPR, which is shown as grey sticks. **b**, Detailed binding between HgmTad2 and 1''-2'-gcADPR. Residues involved in ligand binding are shown as sticks. The red dashed lines represent polar interactions. **c**, ThsA enzyme activity in the presence of 1''-3'-gcADPR and nicotinamide 1,N⁶-ethenoadenine dinucleotide (e-NAD). WT and mutated HgmTad2 at 40 nM were incubated with 5 nM 1''-3'-gcADPR. The reactions were then filtered and their ability to activate ThsA NADase activity was measured. Data are mean \pm s.d. of three independent experiments, with individual datapoints shown. Statistics were calculated in GraphPad Prism using the in-built one-way ANOVA with Dunnett's multiple-comparison test versus

ThsA only. **d**, The overall structure of HgmTad2 tetramer bound to cGG, which is shown as purple sticks. HgmTad2 is shown as a surface model. **e**, Detailed binding between HgmTad2 and cGG. Residues involved in ligand binding are shown as sticks. The red dashed lines represent polar interactions. **f**, Native-PAGE showed the binding of HgmTad2 mutants to cGG. **g**, Native-PAGE showed the binding of HgmTad2 mutants to 1''-2'-gcADPR, 3',3'-cGAMP or cGG. Gel source data for **f** and **g** are provided in Supplementary Fig. 1. **h,i**, The overall structure of HgmTad2 tetramer bound to cGG and 1''-2'-gcADPR simultaneously (**h**), or cGG and 1''-3'-gcADPR simultaneously (**i**). cGG, 1''-2'-gcADPR and 1''-3'-gcADPR are shown as purple, grey and orange sticks, respectively. 2Fo-Fc electron density of the ligands within HgmTad2 tetramer is contoured at 1 σ .

cGG signalling in many bacteria controls motility and biofilm formation³⁹. HgmTad2 is encoded by phages that infect the Gram-negative host *Bacteroides* but, in this organism, these EAL-containing diguanylate cyclases are absent⁴⁰. Instead, cGG signalling is mediated by a CBASS CD-NTase (CdnE) that signals to a TIR- or TM-STING fusion effector protein⁴⁰. After further investigation of the *Bacteroides* and *Sphingobacterium* genomes, which are the bacterial hosts of HgmTad2- and SptTad2-encoding phage, respectively, we found that these bacteria both encode CBASS CD-NTases that are known to produce cGG (CdnE and CdnB)^{22,40} (Extended Data Fig. 1b,c), providing a biologically necessary role for these Tad2 proteins to strongly bind to and sequester cGG signalling molecules. Thus, we tested whether HgmTad2 or SptTad2 can inhibit type I-D^{GG} CBASS immunity that uses cGG signalling molecules with a previously reported TIR-STING activity assay⁴⁰. While NADase activity of TIR-STING from *Sphingobacterium faecium* DSM 11690 could be activated by cGG, its activity was abolished when HgmTad2 or SptTad2 was preincubated with cGG (Fig. 5h). The R31A/N85A and S47A HgmTad2 mutant proteins, which exhibited decreased cGG binding, displayed reduced inhibition of TIR-STING activity (Fig. 5i). Moreover, after proteolysis of HgmTad2, the released cGG again partially activated

the TIR-STING activity (Fig. 5i). These results demonstrate that Tad2 antagonizes type I-D^{GG} CBASS immunity in vitro through sequestering cGG molecules. We further confirmed that Tad2 antagonizes type II-A^{GA} CBASS immunity in vitro (Extended Data Fig. 10a,b).

Despite the Tad2 proteins inhibiting Thoeris activity in vivo (Extended Data Fig. 10c), we did not observe inhibition of the Pa011 type II-A^{GA} CBASS activity in vivo, probably because the 3',3'-cGAMP-binding site is saturated with the highly abundant cGG in *P. aeruginosa* (Extended Data Fig. 10d). We therefore identified a Tad2 homologue derived from a Gammaproteobacteria-infecting phage (GPBTad2). This protein did not bind to cGG in vitro but maintained strong 3',3'-cGAMP binding. When expressed in Pa011, this protein showed inhibition of type II-A^{GA} CBASS (Supplementary Table 2 and Extended Data Fig. 11). These data demonstrate the activity of a versatile anti-CBASS and anti-Thoeris protein family in vitro and in vivo.

Tad2 does not antagonize SpyCas9 activity

We have demonstrated that HgmTad2 could simultaneously inhibit CBASS and Thoeris immunity as a sponge protein with two different

Article

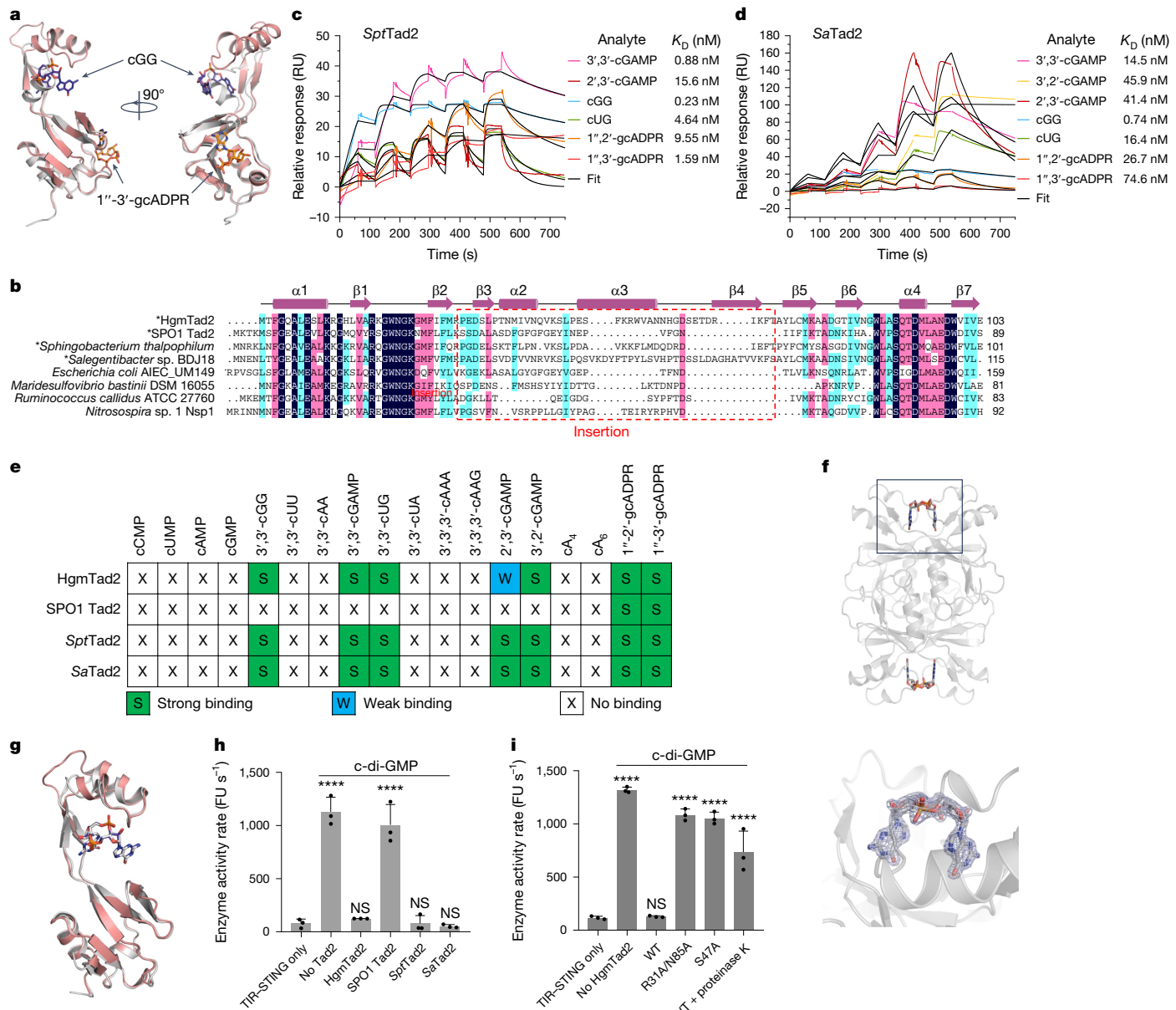


Fig. 5 | Tad2 antagonizes type I-D^{GG} CBASS immunity that uses cGG.

a, Structural superimposition between HgmTad2–cGG–1’-3’-gcADPR and SPO1 Tad2. HgmTad2 is coloured pink. SPO1 Tad2 is coloured grey. **b**, Sequence alignment among Tad2 homologues. Residues with 100% identity, over 75% identity and over 50% identity are shaded in dark blue, pink and cyan, respectively. Secondary structural elements of HgmTad2 are shown above the alignment. The insertion region (residues 32–72) between β 2 and β 5 of HgmTad2 or between β 2 and β 3 of SPO1 Tad2 (residues 36–59) is indicated by a rectangle. Biochemically studied Tad2 homologues are marked with an asterisk before its species name.

binding pockets. However, this very same protein has been previously identified as an anti-CRISPR (Acr) protein, AcrIIA7³⁸, although the inhibitory mechanism is unknown. HgmTad2 (AcrIIA7) was previously shown to not interact with *Streptococcus pyogenes* Cas9 (*SpyCas9*), but somehow inhibited its activity. It was surprising to us that this protein might have three inhibitory activities. Thus, to investigate this activity, we first repeated the *in vitro* *SpyCas9* cleavage assay from the previous study³⁸. Despite many trials and optimization of the reaction system, we still did not see Acr activity of HgmTad2 or the other Tad2 homologues in this study while a control protein, AcrIIA11, successfully inhibits *SpyCas9*-mediated DNA cleavage (Extended Data Fig. 10e). Consistent with this, chromosomal integration of *SpyCas9*

c,d, SPR assay of *SptTad2* (**c**) and *SaTad2* (**d**). **e**, Summary of the binding results of Tad1 homologues. The figure is labelled as in Fig. 2b. **f**, The overall structure of *SptTad2* bound to cGG. A close view of the bound cGG with 2Fo–Fc electron density contoured at 1 σ is shown at the bottom. **g**, Structural superimposition between HgmTad2–cGG and *SptTad2*–cGG. HgmTad2 and cGG are coloured as in **a**. **h,i**, TIR-STING NAD⁺ cleavage activity in the presence of cGG and ϵ -NAD, which emits fluorescence when cleaved. The enzyme activity rate was measured by the accumulation rate of fluorescence units per second. Data are mean \pm s.d. $n = 3$ independent experiments.

into the *P. aeruginosa* strain PAO1 demonstrated that the JBD30 phage is targeted⁴¹, but HgmTad2 did not exhibit Acr activity (Extended Data Fig. 10f). Notably, this experiment is on the same strain background (PAO1) on which HgmTad2 had robust anti-Thoeris activity (Extended Data Fig. 10c). Taken together, our data suggest that HgmTad2 inhibits CBASS and Thoeris, but not the CRISPR–Cas9 system.

Discussion

Thoeris and CBASS are two anti-phage systems that use different signalling molecules to mediate immunity. Two anti-immune proteins, Tad1 and Tad2, have been identified for Thoeris system and two anti-immune

proteins, Acb1 and Acb2, for CBASS. Here we demonstrated that the anti-Thoeris proteins Tad1 and Tad2 also inhibit CBASS systems, which are generally more common, by sequestering a broad array of CDNs and CTNs. Thus, Tad1 and Tad2 are phage-encoded sponge proteins that sequester multiple signalling molecules that are involved in two different anti-phage immune systems. Notably, Tad1 and Tad2 sequester cyclic oligonucleotides with completely distinct mechanisms. One Tad1 hexamer sequesters two CTNs using two separate pockets formed only in the case of the hexameric assembly, in which each pocket is composed of three interlocking protomers. In addition to CTNs, Tad1 also sequesters CDNs using the same binding pocket as gcADPR molecules. By contrast, Tad2 is a tetramer that binds to two CDNs and two gcADPR molecules simultaneously. The binding pocket of CDNs in Tad2 is far from that of gcADPR and is also different from those of other known CDN binding proteins. Notably, both Tad1 and Tad2 sequester 3',2'-cGAMP, a signalling molecule that is not cleaved by Acb1, but has been recently implicated in both CBASS and cGAS-like signalling systems in eukaryotes^{23,42,43}.

CTNs are used by many CBASS systems and some type III CRISPR–Cas systems (using cA₃, but also cA₄ and cA₆, to activate effectors^{44–47}) to stop phage infection⁴⁴. Thus, Tad1 may also inhibit type III CRISPR–Cas systems relying on cA₃. Both Tad1 and Acb2 can antagonize CTN signalling, although this was not the originally identified function for either. While the binding mode of CTNs is similar between Tad1 and Acb2, the assembly mechanism of the hexamer and residues involved in binding are different between these proteins⁸. As bacterial species can contain multiple signalling defence systems^{14,29}, the pressure for multifunctional inhibitors has emerged, with Tad1 and Tad2 representing a unique class of proteins that inhibit more than one defence system. Together, our findings demonstrate the considerable potency of two anti-immune sponge proteins. Together with data on Acb2, these data on Tad1 and Tad2 establish a paradigm of anti-immune sponge proteins having more than one binding site. We predict that a broad distribution of anti-immune sponges with multiple binding sites for signalling molecules may exist for anti-viral immune signalling systems across all domains of life.

Online content

Any methods, additional references, Nature Portfolio reporting summaries, source data, extended data, supplementary information, acknowledgements, peer review information; details of author contributions and competing interests; and statements of data and code availability are available at <https://doi.org/10.1038/s41586-024-08122-4>.

- Manik, M. K. et al. Cyclic ADP ribose isomers: production, chemical structures, and immune signaling. *Science* **377**, eadc8969 (2022).
- Ofir, G. et al. Antiviral activity of bacterial TIR domains via immune signalling molecules. *Nature* **600**, 116–120 (2021).
- Cohen, D. et al. Cyclic GMP-AMP signalling protects bacteria against viral infection. *Nature* **574**, 691–695 (2019).
- Leavitt, A. et al. Viruses inhibit TIR gcADPR signaling to overcome bacterial defense. *Nature* **611**, 326–331 (2022).
- Yirmiya, E. et al. Phages overcome bacterial immunity via diverse anti-defense proteins. *Nature* **625**, 352–359 (2024).
- Huiting, E. et al. Bacteriophages inhibit and evade cGAS-like immune function in bacteria. *Cell* **186**, 864–876 (2023).
- Jenson, J. M., Li, T., Du, F., Ea, C. K. & Chen, Z. J. Ubiquitin-like conjugation by bacterial cGAS enhances anti-phage defence. *Nature* **616**, 326–331 (2023).
- Cao, X. et al. Phage anti-CBASS protein simultaneously sequesters cyclic tri nucleotides and dinucleotides. *Mol. Cell* **84**, 375–385 (2024).
- Doron, S. et al. Systematic discovery of antiphage defense systems in the microbial pan genome. *Science* **359**, eaar4120 (2018).
- Gao, L. et al. Diverse enzymatic activities mediate antiviral immunity in prokaryotes. *Science* **369**, 1077–1084 (2020).
- Millman, A. et al. An expanded arsenal of immune systems that protect bacteria from phages. *Cell Host Microbe* **30**, 1556–1569 (2022).
- Rousset, F. et al. Phages and their satellites encode hotspots of antiviral systems. *Cell Host Microbe* **30**, 740–753 (2022).
- Vassallo, C. N., Doering, C. R., Littlehale, M. L., Teodoro, G. I. C. & Laub, M. T. A functional selection reveals previously undetected anti-phage defence systems in the *E. coli* pan genome. *Nat. Microbiol.* **7**, 1568–1579 (2022).
- Johnson, M. C. et al. Core defense hotspots within *Pseudomonas aeruginosa* are a consistent and rich source of anti-phage defense systems. *Nucleic Acids Res.* **51**, 4995–5005 (2023).
- Stanley, S. Y. & Maxwell, K. L. Phage-encoded anti-CRISPR defenses. *Annu. Rev. Genet.* **52**, 445–464 (2018).
- Li, Y. & Bondy-Denomy, J. Anti-CRISPRs go viral: the infection biology of CRISPR-Cas inhibitors. *Cell Host Microbe* **29**, 704–714 (2021).
- Jia, N. & Patel, D. J. Structure-based functional mechanisms and biotechnology applications of anti-CRISPR proteins. *Nat. Rev. Mol. Cell Biol.* **22**, 563–579 (2021).
- Davidson, A. R. et al. Anti-CRISPRs: protein inhibitors of CRISPR-Cas systems. *Annu. Rev. Biochem.* **89**, 309–332 (2020).
- Gao, Z. & Feng, Y. Bacteriophage strategies for overcoming host antiviral immunity. *Front. Microbiol.* **14**, 1211793 (2023).
- Hobbs, S. J. et al. Phage anti-CBASS and anti-Pycsar nucleases subvert bacterial immunity. *Nature* **605**, 522–526 (2022).
- Athukoralage, J. S. et al. An anti-CRISPR viral ring nuclease subverts type III CRISPR immunity. *Nature* **577**, 572–575 (2020).
- Whiteley, A. T. et al. Bacterial cGAS-like enzymes synthesize diverse nucleotide signals. *Nature* **567**, 194–199 (2019).
- Fatma, S., Chakravarti, A., Zeng, X. & Huang, R. H. Molecular mechanisms of the CdnG-Cap5 antiphage defense system employing 3',2'-cGAMP as the second messenger. *Nat. Commun.* **12**, 6381 (2021).
- Millman, A., Melamed, S., Amitai, G. & Sorek, R. Diversity and classification of cyclic-oligonucleotide-based anti-phage signalling systems. *Nat. Microbiol.* **5**, 1608–1615 (2020).
- Burroughs, A. M., Zhang, D., Schäffer, D. E., Iyer, L. M. & Aravind, L. Comparative genomic analyses reveal a vast, novel network of nucleotide-centric systems in biological conflicts, immunity and signaling. *Nucleic Acids Res.* **43**, 10633–10654 (2015).
- Davies, B. W., Bogard, R. W., Young, T. S. & Mekalanos, J. J. Coordinated regulation of accessory genetic elements produces cyclic di-nucleotides for *V. cholerae* virulence. *Cell* **149**, 358–370 (2012).
- Duncan-Lowey, B., McNamara-Bordewick, N. K., Tal, N., Sorek, R. & Kranzusch, P. J. Effector-mediated membrane disruption controls cell death in CBASS antiphage defense. *Mol. Cell* **81**, 5039–5051 (2021).
- Tesson, F. et al. Systematic and quantitative view of the antiviral arsenal of prokaryotes. *Nat. Commun.* **13**, 2561 (2022).
- Wu, Y. et al. Bacterial defense systems exhibit synergistic anti-phage activity. *Cell Host Microbe* **32**, 557–572 (2024).
- van Beljouw, S. P. B., Sanders, J., Rodriguez-Molina, A. & Brouns, S. J. J. RNA-targeting CRISPR-Cas systems. *Nat. Rev. Microbiol.* **21**, 21–34 (2022).
- Tal, N. et al. Cyclic CMP and cyclic UMP mediate bacterial immunity against phages. *Cell* **184**, 5728–5739 (2021).
- Molina, R., Sofos, N. & Montoya, G. Structural basis of CRISPR-Cas type III prokaryotic defence systems. *Curr. Opin. Struct. Biol.* **65**, 119–129 (2020).
- Lau, R. K. et al. Structure and mechanism of a cyclic trinucleotide-activated bacterial endonuclease mediating bacteriophage immunity. *Mol. Cell* **77**, 723–733 (2020).
- Ye, Q. et al. HORMA domain proteins and a Trip13-like ATPase regulate bacterial cGAS-like enzymes to mediate bacteriophage immunity. *Mol. Cell* **77**, 709–722 (2020).
- Thomas, J. A. et al. Extensive proteolysis of head and inner body proteins by a morphogenetic protease in the giant *Pseudomonas aeruginosa* phage φKZ. *Mol. Microbiol.* **84**, 324–339 (2012).
- Fossati, A. et al. Next-generation proteomics for quantitative Jumbophage-bacteria interaction mapping. *Nat. Commun.* **14**, 5156 (2023).
- Guan, J. et al. Bacteriophage genome engineering with CRISPR-Cas13a. *Nat. Microbiol.* **7**, 1956–1966 (2022).
- Uribe, R. V. et al. Discovery and characterization of Cas9 inhibitors disseminated across seven bacterial phyla. *Cell Host Microbe* **25**, 233–241 (2019).
- Jenal, U., Reinders, A. & Lori, C. Cyclic di-GMP: second messenger extraordinaire. *Nat. Rev. Microbiol.* **15**, 271–284 (2017).
- Morehouse, B. R. et al. STING cyclic dinucleotide sensing originated in bacteria. *Nature* **586**, 429–433 (2020).
- Mahendra, C. et al. Broad-spectrum anti-CRISPR proteins facilitate horizontal gene transfer. *Nat. Microbiol.* **5**, 620–629 (2020).
- Slavik, K. M. et al. cGAS-like receptors sense RNA and control 3'2'-cGAMP signalling in *Drosophila*. *Nature* **597**, 109–113 (2021).
- Cai, H. et al. The virus-induced cyclic dinucleotide 2'3'-c-di-GMP mediates STING-dependent antiviral immunity in *Drosophila*. *Immunity* **56**, 1991–2005 (2023).
- Grüschow, S., Adamson, C. S. & White, M. F. Specificity and sensitivity of an RNA targeting type III CRISPR complex coupled with a NucC endonuclease effector. *Nucleic Acids Res.* **49**, 13122–13134 (2021).
- McMahon, S. A. et al. Structure and mechanism of a type III CRISPR defence DNA nuclelease activated by cyclic oligoadenylate. *Nat. Commun.* **11**, 500 (2020).
- Niewohner, O. et al. Type III CRISPR–Cas systems produce cyclic oligoadenylate second messengers. *Nature* **548**, 543–548 (2017).
- Kazlauskienė, M., Kostiuč, G., Venclavas, Č., Tamulaitis, G. & Siksnys, V. A. Cyclic oligonucleotide signaling pathway in type III CRISPR–Cas systems. *Science* **357**, 605–609 (2017).

Publisher's note Springer Nature remains neutral with regard to jurisdictional claims in published maps and institutional affiliations.

Springer Nature or its licensor (e.g. a society or other partner) holds exclusive rights to this article under a publishing agreement with the author(s) or other rightsholder(s); author self-archiving of the accepted manuscript version of this article is solely governed by the terms of such publishing agreement and applicable law.

© The Author(s), under exclusive licence to Springer Nature Limited 2024

Methods

Bacterial strains and phages

The *P. aeruginosa* strains (BWHP5A011, ATCC 27853, MRSN390231, PAO1) and *E. coli* strains (DH5 α) were grown in lysogeny broth (LB) medium at 37 °C both with aeration at 225 rpm. Bacteria plating was performed on LB broth supplemented with gentamicin for maintaining pHERD30T plasmid (50 μ g ml $^{-1}$ for *P. aeruginosa* and 20 μ g ml $^{-1}$ for *E. coli*), as well as with 10 mM MgSO $_4$ for phage spot assays. Gene expression in *P. aeruginosa* was induced by the addition of 0.2–0.3% L-arabinose or 0.3 mM isopropyl-β-D-thiogalactopyranoside (IPTG) unless stated otherwise. The *E. coli* BL21(DE3) strain was used for recombinant protein overexpression and grown in LB medium. The cells were grown at 37 °C until the optical density at 600 nm (OD $_{600}$) reached 0.8 and were then induced at 18 °C for 12 h.

Protein expression and purification

The *C. botulinum* Tad1, *C. mangenotii* Tad1, SBSphij7 Tad1, *Colidexitribacter* Tad1, *S. thalpophilum* Tad2, *Salegentibacter* sp. BDJ18 Tad2, SPO1 Tad2, *P. aeruginosa* BWHP5A011 CapV, *P. aeruginosa* ATCC 27853 NucC, *B. cereus* MSX-D12 ThsA, *S. faecium* DSM 11690 STING and *S. pyogenes* Cas9 genes were synthesized by GenScript and codon-optimized for expression in *E. coli*. The full-length *Cm*Tad1, SBS Tad1, ColiTad1, SptTad2, *Sa*Tad2, *Ec*Tad2, ThsA, CapV, NucC, *Sf*STING and SpyCas9 gene was amplified by PCR and cloned into a modified pET28a vector in which the expressed protein contains a His6 tag or His6-SUMO tag. The full-length *Cb*Tad1 gene was amplified by PCR and cloned into a modified pRSFDuet vector in which the expressed *Cb*Tad1 protein contains a His6 tag. The Tad1 or Tad2 mutants were generated by two-step PCR and were subcloned, overexpressed and purified in the same way as for the WT protein. All of the proteins were expressed in *E. coli* strain BL21(DE3) and induced by 0.2 mM IPTG when the cell density reached an OD $_{600}$ of 0.8. After growth at 18 °C for 12 h, the cells were collected, resuspended in lysis buffer (50 mM Tris-HCl pH 8.0, 300 mM NaCl, 10 mM imidazole and 1 mM PMSF) and lysed by sonication. The cell lysate was centrifuged at 20,000g for 50 min at 4 °C to remove cell debris. The supernatant was applied onto a self-packaged Ni-affinity column (2 ml Ni-NTA, Genscript) and contaminant proteins were removed with wash buffer (50 mM Tris pH 8.0, 300 mM NaCl, 30 mM imidazole). The protein was then eluted with elute buffer (50 mM Tris pH 8.0, 300 mM NaCl, 300 mM imidazole). The eluate of protein was concentrated and further purified using a Superdex-200 increase 10/300 GL (GE Healthcare) column equilibrated with a buffer containing 10 mM Tris-HCl pH 8.0, 200 mM NaCl and 5 mM DTT. The purified proteins were analysed by SDS-PAGE. The fractions containing the target protein were pooled and concentrated. Specifically, SBS Tad1 was purified using the same approach as described above, but the buffer pH was 8.8, with 500 mM NaCl and 10% glycerol throughout the whole purification process.

The cells expressing CapV were resuspended with lysis buffer containing 50 mM phosphate buffer pH 7.4, 300 mM NaCl, 10% glycerol (v/v). The CapV proteins bound to Ni-NTA beads were washed with a buffer containing 50 mM phosphate buffer pH 7.4, 300 mM NaCl, 10% glycerol (v/v), 30 mM imidazole and then eluted with the 50 mM phosphate buffer pH 7.4, 300 mM NaCl, 10% glycerol (v/v) and 300 mM imidazole. The eluate of CapV was concentrated and further purified using a Superdex-200 increase 10/300 GL (GE Healthcare) column equilibrated with a reaction buffer containing 50 mM phosphate buffer pH 7.4, 300 mM NaCl, 10% glycerol (v/v). The purified protein was analysed as described above. The fusion protein of NucC with His6-SUMO tag was digested with Ulp1 on the Ni-NTA column at 18 °C for 2 h after removing contaminant proteins with wash buffer. The NucC protein was then eluted with wash buffer. The eluate of NucC was concentrated and further purified as His-tagged proteins as described above.

The full-length genes encoding HgmTad2 and AcrlIA11 were synthesized by GenScript and amplified by PCR and cloned into pGEX6p-1 to

produce a GST-tagged fusion protein with a PreScission Protease cleavage site between GST and the target protein. The HgmTad2 mutants were subcloned, overexpressed and purified in the same way as for the WT protein. The proteins were expressed and induced similarly as above. After growth at 16 °C for 12 h, the cells were collected, resuspended in lysis buffer (1× PBS, 2 mM DTT and 1 mM PMSF) and lysed by sonication. The cell lysate was centrifuged at 18,000g for 50 min at 4 °C to remove cell debris. The supernatant was applied onto a self-packaged GST-affinity column (2 ml glutathione Sepharose 4B; GE Healthcare) and contaminant proteins were removed with wash buffer (1× PBS and 2 mM DTT). The fusion protein was then digested with PreScission protease at 16 °C for 2 h. The protein with an additional five-amino-acid tag (GPLGS) at the N terminus was eluted with buffer containing 25 mM HEPES pH 7.5, 200 mM NaCl and 2 mM DTT. The eluate was concentrated and further purified using the Superdex-200 (GE Healthcare) column equilibrated with a buffer containing 10 mM Tris-HCl pH 8.0, 200 mM NaCl and 5 mM DTT. Next, the HgmTad2 protein was desalted into QA buffer containing 25 mM Tris pH 8.0, 10 mM NaCl and 2 mM DTT by a desalting column (GE Healthcare), and was further purified by ion-exchange chromatography using the Resource Q column (GE Healthcare). The protein bound to the column was eluted with a gradient concentration of 10–100 mM NaCl, and the protein purity and states were then verified using native-PAGE and SDS-PAGE, respectively, together with the protein sample flowed through the column. Selenomethionine (Se-Met)-labelled HgmTad2 was expressed in *E. coli* B834 (DE3) cells grown in M9 minimal medium supplemented with 60 mg l $^{-1}$ SeMet (Acros) and specific amino acids: Ile, Leu and Val at 50 mg l $^{-1}$; Lys, Phe and Thr at 100 mg l $^{-1}$. The SeMet protein was purified as described above. The four Acb2 homologues were cloned and purified as described previously 8 . The sequences of proteins used in this study are provided in Supplementary Table 3.

Crystallization

All of the protein samples in this study were diluted in buffer containing 10 mM Tris-HCl pH 8.0, 200 mM NaCl and 5 mM DTT before crystallization. Each protein was crystallized at 18 °C using the following conditions:

- (1) Apo *Cm*Tad1 and HgmTad2: the concentration of both proteins was 30 mg ml $^{-1}$. The crystals of *Cm*Tad1 were grown for 3–4 days using a reservoir solution containing 2.0 M ammonium sulfate, 0.1 M sodium HEPES pH 7.5 and 1.4% (v/v) PEG 400. The crystals of HgmTad2 were grown for 2–3 days using a reservoir solution containing 1.0 M lithium chloride, 0.1 M citrate pH 4.0, 20% (w/v) PEG 6000. Before being collected, the crystals were cryoprotected in the reservoir solution containing 20% glycerol before flash-freezing in liquid nitrogen.
- (2) *Cm*Tad1 in a complex with cA $_3$ or cAAG, and *Cb*Tad1 in a complex with cA $_3$ /2',3'-cGAMP-cA $_3$: before crystallization, cA $_3$ or cAAG was mixed with protein at a molar ratio of 0.8:1, and 2',3'-cGAMP was mixed with protein at a molar ratio of 1.2:1. The crystals of *Cm*Tad1-cA $_3$ and *Cm*Tad1-cAAG grew to full size in about 4–5 days, their reservoir solution contains 1.6 M ammonium sulfate, 10% (v/v) 1,4-dioxane. The crystallization condition of *Cb*Tad1-cA $_3$ was 0.1 M MIB (sodium malonate dibasic monohydrate, imidazole, boric acid) pH 6.0, 55% (v/v) MPD and the crystallization condition of the *Cb*Tad1-cA $_3$ was 0.1 M PCTP (sodium propionate, sodium cacodylate trihydrate, Bis-Tris propane) pH 8.0, 60% MPD.
- (3) *Cb*Tad1 in a complex with 1''-3'-gcADPR or 1''-3'-gcADPR-cA $_3$: *Cb*Tad1 co-expressed with ThsB' was purified, and was then mixed with cA $_3$ at a molar ratio of 1:0.8. The crystals of purified *Cb*Tad1 or its mix with cA $_3$ were grown in a reservoir solution containing 3.2 M ammonium sulfate and 0.1 M citrate pH 5.0 for 4–5 days. They were stored in antifreeze containing 20% glycerol and quick-frozen with liquid nitrogen.

- (4) HgmTad2 in a complex with cGG, 1''-2'-gcADPR, 1''-2'-gcADPR-cGG or 3',3'-cGAMP: these four structures were crystallized under the same conditions containing 1.0 M lithium chloride, 0.1 M citrate pH 4.0 and 20% (w/v) PEG 6000. For HgmTad2 in a complex with cGG, purified HgmTad2 in the cGG-bound state was used. For HgmTad2 in a complex with 1''-2'-gcADPR or 1''-2'-gcADPR-cGG, HgmTad2 co-expressed with BdTIR (TIR protein from *Brachypodium distachyon*) was purified, and the no-cGG or cGG-bound form was used, respectively. For HgmTad2 in a complex with 3',3'-cGAMP, HgmTad2 in the no-cGG state was used and mixed with 3',3'-cGAMP at a molar ratio of 1:1.2.
- (5) HgmTad2 in a complex with 1''-3'-gcADPR-cGG: HgmTad2 co-expressed with ThsB' (ThsB' protein from *B. cereus* MSX-D12⁴) was purified and the cGG-bound form was used in crystallization. The crystallization condition was 0.2 M ammonium sulfate, 0.1 M sodium acetate trihydrate pH 4.6 and 25% (w/v) PEG 4000.
- (6) Apo SPO1Tad2: after purifying SPO1Tad2, the protein was diluted to 24 mg ml⁻¹, and then grown under conditions with 0.5 M ammonium sulfate, 1.0 M sodium citrate tribasic dihydrate pH 5.6, 1.0 M lithium sulfate monohydrate conditions for about 1 week.
- (7) *SptTad2*-cGG: the *SptTad2* protein purified from *E. coli* BL-21 naturally carries c-di-GMP. The protein was diluted to 24 mg ml⁻¹, and then grown under conditions containing 0.3 M magnesium nitrate hexahydrate, 0.1 M Tris pH 8.0, 23% (w/v) PEG 2000 for 4–5 days, transferred into antifreeze and then flash-frozen in liquid nitrogen.

Data collection, structure determination and refinement

All data were collected at SSRF beamlines BL02U1 and BL19U1, integrated and scaled using the HKL2000 package⁴⁸. The initial model of *CbTad1* was used from Protein Data Bank (PDB) 7UAV. The initial models of *CmTad1*, SPO Tad2 and *SptTad2* were obtained using AlphaFold2⁴⁹. The structure of apo HgmTad2 was solved by SAD phasing using Autosol in PHENIX⁵⁰. The structures of protein in complexes with cyclic oligonucleotides were solved through molecular replacement and refined manually using COOT⁵¹. All of the structures were further refined with PHENIX⁵⁰ using non-crystallographic symmetry and stereochemistry information as restraints. The final structure was obtained through several rounds of refinement. Final Ramachandran statistics: 96.75% favoured, 3.25% allowed and 0% outliers for the apo *CmTad1*-Zn structure; 96.62% favoured, 3.38% allowed and 0% outliers for *CmTad1*-Zn-cA₃; 96.75% favoured, 3.25% allowed and 0% outliers for the *CmTad1*-Zn-cAAG structure; 97.59% favoured, 2.41% allowed and 0% outliers for the *CbTad1*-1''-3'-gcADPR structure; 96.37% favoured, 3.63% allowed and 0% outliers for the *CbTad1*-1''-3'-gcADPR-cA₃ structure; 96.99% favoured, 3.01% allowed and 0% outliers for the *CbTad1*-2',3'-cGAMP structure; 97.82% favoured, 2.18% allowed and 0% outliers for the *CbTad1*-2',3'-cGAMP-cA₃ structure; 97.55% favoured, 2.45% allowed and 0% outliers for the apo HgmTad2 structure; 96.32% favoured, 3.68% allowed and 0% outliers for the HgmTad2-1''-2'-gcADPR structure; 95.34% favoured, 4.66% allowed and 0% outliers for the HgmTad2-1''-2'-gcADPR-cGG structure; 97.06% favoured, 2.94% allowed and 0% outliers for the HgmTad2-1''-3'-gcADPR-cGG structure; 97.06% favoured, 2.94% allowed and 0% outliers for the HgmTad2-1''-2'-gcADPR-cGG structure; 98.77% favoured, 1.23% allowed and 0% outliers for the HgmTad2-3',3'-cGAMP structure; 97.98% favoured, 2.02% allowed and 0% outliers for the *SptTad2*-cGG structure; 98.63% favoured, 1.37 allowed and 0% outliers for apo SPO1 Tad2 structure. Structural illustrations were generated using PyMOL (<https://pymol.org/>). Data collection and structure refinement statistics are summarized in Extended Data Table 1.

ITC binding assay

The dissociation constants of binding reactions of *CmTad1* or *CbTad1* with cA₃, cAAG, 3',2'-cGAMP, 2',3'-cGAMP, 3',3'-cGAMP, cAA, cGG, cUG, cUA or cUU, of SBS Tad1 with cA₃, cAAG, 3',2'-cGAMP, 2',3'-cGAMP, 3',3'-cGAMP, cUA, 1''-2'-gcADPR or 1''-3'-gcADPR, and of ColiTad1 with

cA₃, cAAG, 3',2'-cGAMP, 2',3'-cGAMP or 3',3'-cGAMP were determined by ITC using a MicroCal ITC200 calorimeter. All of the protein and cyclic oligonucleotides were desalted into the working buffer containing 20 mM HEPES pH 7.5 and 200 mM NaCl. The titration, for example, was carried out with 19 successive injections of 2 µl cA₃ or cAAG at 25 µM concentration, spaced 120 s apart, into the sample cell containing *CbTad1* with a concentration of 5 µM by 700 rpm at 25 °C. Correspondingly, 3',2'-cGAMP or 2',3'-cGAMP at 150 µM concentration was titrated into 50 µM *CbTad1*. cA₃ or cAAG at 150 µM concentration was titrated into 30 µM *CmTad1*, and 3',2'-cGAMP, 2',3'-cGAMP, 3',3'-cGAMP, cAA, cGG, cUG, cUA or cUU at 300 µM concentration was titrated into 100 µM *CmTad1*. For SBS Tad1, 3',2'-cGAMP, 3',3'-cGAMP, 2',3'-cGAMP, cUA, 1''-2'-gcADPR or 1''-3'-gcADPR at 300 µM concentration was titrated into 100 µM SBS Tad1, and 3',2'-cGAMP, 3',3'-cGAMP or 2',3'-cGAMP at 300 µM concentration was titrated into 100 µM ColiTad1. For both SBS Tad1 and ColiTad1, cA₃ or cAAG at 150 µM concentration was titrated into 30 µM SBS Tad1 or ColiTad1. All of the above titration experiments were performed using the same experimental procedure. The Origin software was used for baseline correction, integration and curve fitting to a single site binding model.

ThsA NADase activity assay

The NADase assay was performed using ThsA enzyme from *B. cereus* MSX-D12, which was expressed and purified as described previously, as a reporter for the presence of cyclic ADPR isomers. The NADase reaction was performed in a black 96-well plate (Corning 96-well half area black non-treated plate with a flat bottom) at 37 °C in a 95 µl reaction volume, and the final concentration of ThsA and 1''-3'-gcADPR was 50 nM and 5 nM, respectively. Next, 5 µl of 2 mM ε-NAD solution was added to each well immediately before measurement and mixed by pipetting rapidly. ε-NAD was used as a fluorogenic substrate to report ThsA enzyme NADase activity by monitoring increase in fluorescence (excitation 300 nm, emission 410 nm) using the EnSpire Multimode Plate Reader (PerkinElmer) at 37 °C. To examine the inhibitory effect of HgmTad2 or its mutants on ThsA, HgmTad2 or its mutants (40 nM of each) was incubated with 5 nM 1''-3'-gcADPR in incubation buffer (50 mM Tris pH 7.5 and 50 mM NaCl) at room temperature for 5 min in advance. ThsA was then added at a final concentration of 50 nM. After an incubation for 5 min, ε-NAD was added to start the reaction.

SPR assay

The SPR analysis was performed using a Biacore 8K (GE Healthcare) at room temperature (25 °C). Equal concentrations of HgmTad2, SPO1 Tad2, *SptTad2* and *SaTad2* were immobilized on channels of the carboxymethyldextran-modified (CMS) sensor chip to about 280 response units (RU). To collect data for kinetic analysis, a series of concentrations (12.5 nM, 25 nM, 50 nM, 100 nM and 200 nM) of 3',3'-cGAMP, 3',2'-cGAMP, 2',3'-cGAMP, cGG and cUG/cA₃, diluted in binding buffer (20 mM HEPES pH 7.5, 200 mM NaCl and 0.05% (v/v) Tween-20), was injected over the chip at a flow rate of 30 µl min⁻¹. The protein-ligand complex was allowed to associate for 60 s and dissociate for 600 s. Data were fit with a model describing a bivalent analyte. Kinetic rate constants were extracted from this curve fit using Biacore evaluation software (GE Healthcare).

HPLC analysis

For analysis of ligand sequestering, 40 µM Tad1 or Tad2 protein was pre-incubated with 4 µM cA₃, 2',3'-cGAMP or 3',3'-cGAMP for 30 min at 18 °C. Next, for Tad1 series, proteinase K was subsequently added to the reaction system at a final concentration of 0.5 µM and the reaction was performed at 58 °C for 1 h. For Tad2, the sample was first heated at 100 °C for 10 min, and then proteinase K was subsequently added to the reaction system at a final concentration of 25 µM and the reaction was performed at 58 °C for 3 h. For analysis of intrinsically bound nucleotide in HgmTad2 during expression, 40 µM HgmTad2 in different

Article

states was treated as reported for Tad2 in the above. 4 μ M 3',3'-cGAMP and cGG were used as standards.

The reaction samples were transferred to Amicon Ultra-15 Centrifugal Filter Unit 3 kDa and centrifuged at 4 °C, 4,000g. The products obtained by filtration were further filtered with a 0.22 μ m filter and were subsequently used for HPLC experiments. The HPLC analysis was performed on the Agilent 1200 system with a ZORBAX Bonus-RP column (4.6 \times 150 mm). A mixture of 2% acetonitrile and 0.1% trifluoroacetic acid solution in water (98%) was used as the mobile phase with 0.8 ml min⁻¹. For cA₃, 5% acetonitrile and 0.1% trifluoroacetic acid solution in water (95%) was used as the mobile phase. The compounds were detected at 254 nm.

Fluorogenic biochemical assay

The enzymatic reaction velocity was measured as previously described⁶. In brief, the esterase activity of the 6 \times His-tagged CapV was probed with the fluorogenic substrate resorufin butyrate, which is a phospholipase substrate that emits fluorescence when hydrolysed. The CapV protein was diluted in 50 mM sodium phosphate pH 7.4, 300 mM NaCl, 10% (v/v) glycerol to a final concentration of 2 μ M. To determine the enzymatic activity of CapV activated by 3',3'-cGAMP, 0.8 μ M of 3',3'-cGAMP was added to DMSO solubilized resorufin butyrate (stock of 20 mM mixed with 50 mM sodium phosphate pH 7.4, 300 mM NaCl, 10% (v/v) glycerol reaching a final concentration of 100 μ M). Subsequently, the purified 6 \times His-tagged CapV was added to the reaction solution containing 3',3'-cGAMP to a final assay volume of 50 μ l, and fluorescence was measured in a 96-well plate (Corning 96-well half area black non-treated plate with a flat bottom). Plates were read once every 30 s for 10 min at 37 °C using a EnSpire Multimode Plate Reader (PerkinElmer) with excitation and emission wavelengths of 550 and 591 nm, respectively.

To determine the function of inhibitory proteins, 8 μ M protein was pre-incubated with 0.8 μ M 3',3'-cGAMP for 10 min at 18 °C, and the subsequent detection method was as described above. To examine whether the released molecule from HgmTad2 or SBS Tad1 is still able to activate CapV, 0.8 μ M 3',3'-cGAMP was incubated with 8 μ M HgmTad2 or SBS Tad1 for 10 min at 18 °C. Proteinase K was subsequently added to the reaction system at a final concentration of 25 μ M and the reaction was performed at 58 °C for 3 h. Reaction products were transferred to Amicon Ultra-4 Centrifugal Filter Unit 3 kDa and centrifuged at 4 °C, 4,000g. Filtered products were used for CapV activity assay as described above.

SfTIR-STING NAD⁺ enzyme activity assay

The enzymatic reaction velocity was measured as previously described⁴⁰. The enzymatic activity of SfTIR-STING was activated by cGG. 500 μ M ϵ -NAD and 50 nM cGG were mixed in a 96-well plate format with reaction buffer (50 mM Tris pH 7.5, 50 mM NaCl). Subsequently, purified 6 \times His-tagged SfTIR-STING was added to the reaction to a final assay volume of 50 μ l and plates were read once every 15 s for 10 min at 37 °C using the EnSpire Multimode Plate Reader (PerkinElmer) with excitation and emission wavelengths of 410 and 300 nm, respectively. The reaction rate was calculated from the linear part of the initial reaction.

To determine the function of inhibitory proteins, 1 μ M HgmTad2, SPO1 Tad2, SptTad2 and SaTad2 were pre-incubated with 50 nM cGG for 20 min at 18 °C, and the subsequent detection method was as described above. To determine the function of HgmTad2 mutants, 200 nM HgmTad2 and its mutants was pre-incubated with 50 nM cGG for 20 min at 18 °C. To examine whether the released molecule from HgmTad2 is still able to activate SfTIR-STING, 50 nM cGG was incubated with 200 nM HgmTad2 for 10 min at 18 °C. Proteinase K was subsequently added to the reaction system at a final concentration of 1 μ M and the reaction was performed at 58 °C for 1 h. The reaction products were transferred to the Amicon Ultra-4 Centrifugal Filter Unit 3 kDa and centrifuged at 4 °C, 4,000g. Filtered products were used for SfSTING activity assay as described above.

In vitro NucC activity assay

The nuclease activity assay was measured as previously described⁸. The pUC19 plasmid was used as the substrate. NucC (10 nM) and cA₃ molecules (5 nM) were mixed with 0.4 μ g DNA in a buffer containing 25 mM Tris-HCl pH 8.0, 10 mM NaCl, 10 mM MgCl₂ and 2 mM DTT (20 μ l reaction volume), incubated at 37 °C for 20 min, then separated on a 1% agarose gel. Gels were stained with Goldview and imaged by ultraviolet illumination.

To determine the function of CbTad1, 200 nM CbTad1 or its mutants was pre-incubated with the other components at 18 °C for 30 min, and the subsequent reaction and detection method was performed as described above. To examine whether the released molecule from CbTad1 is able to activate NucC, 5 nM cA₃ was incubated with 200 nM CbTad1 at 18 °C for 20 min. Proteinase K was subsequently added to the reaction system at a final concentration of 1 μ M and the reaction was performed at 58 °C for 1 h, the proteinase K-treated samples were then heated with 100 °C for 10 min to extinguish proteinase K and the subsequent detection method was performed as described above.

In vitro SpyCas9 DNA cleavage assay

SpyCas9 sgRNA was generated using the in vitro T7 transcription kit (Vazyme). A total of 100 nM SpyCas9 and 150 nM sgRNA was incubated with 10 μ M purified Tad2 or AcrlIA11 in cleavage buffer (20 mM HEPES-KOH pH 7.5, 75 mM KCl, 10% glycerol, 1 mM DTT and 10 mM MgCl₂) for 30 min at 37 °C. Plasmid pUC57 containing the target protospacer 25 sequence inserted using KpnI/XbaI was linearized by ScaI digestion. Linearized plasmid was added to the Cas9-sgRNA complex at a 10 nM final concentration. The reactions were incubated at 37 °C for 10 min and extinguished by 1 μ M proteinase K for 15 min at 58 °C, then separated on a 1% agarose gel. Gels were stained with Goldview and imaged by ultraviolet illumination.

SpyCas9 sgRNA DNA template. ATGTAATACGACTCACTATAGG AAATTAGGTGCGCTTGGCGTTTAGAGCTAGAAATAGCAAGTAAAAA TAAGGCTAGTCGTTATCAACTGAAAAAGTGGCACCGAGTCGGTGCTT.

Cleavage assay DNA sequence. TCGGTGCGGGCTCTTCGCTA TTACGCCAGCTGGCGAAAGGGGGATGTGCTGCAAGGCAGTTAAGTT GGTAACGCCAGGGTTTCCCACTCAGCAGCGTTGAAACGACGCCA GTGCCAACGCTTGCATGCCGCAGGTCGACTCTAGAGGATCCCAATCCC AGCCAAGCGCACCTAATTCCGAATTGTAATCATGGTCATAGCTGTT TCCTGTGAAATTGTTATCCGCTACAATTCCACACAAACATACGAGCC GGAAGCATAAA.

Native-PAGE assay

For ligand binding native-PAGE assay, proteins were pre-incubated with cyclic nucleotides for 20 min at 18 °C, where protein was 20 μ M and the concentrations of cyclic nucleotides was 5, 10 or 20 μ M, respectively. Products of the reaction were analysed using 5% native polyacrylamide gels and visualized by Coomassie blue staining.

Multi-angle light scattering

Multi-angle light scattering experiments were performed in 10 mM Tris pH 8.0, 200 mM NaCl and 2 mM TCEP using the Superdex-200 10/300 GL size-exclusion column from GE Healthcare. All protein concentrations were diluted to 1.7 mg ml⁻¹. The chromatography system was connected to the Wyatt DAWN HELEOS Laser photometer and a Wyatt Optilab T-rEX differential refractometer. Wyatt ASTRA v.7.3.2 software was used for data analysis.

Episomal gene expression

The shuttle vector pHERD30T, which replicates in *P. aeruginosa* and *E. coli*⁵², was used for episomal expression of Acb2 and Tad proteins in *P. aeruginosa* strains. pHERD30T has an arabinose-inducible promoter

and a selectable gentamicin marker. The vector was digested with NcoI and HindIII restriction enzymes. Inserts were amplified by PCR using bacterial overnight culture or synthesized by Twist Bioscience and joined with the digested vector using Hi-Fi DNA Gibson Assembly (NEB) according to the manufacturer's protocol. The resulting plasmids were transformed into *E. coli* DH5α. All plasmid constructs were verified by whole plasmid sequencing. *P. aeruginosa* cells were electroporated with the pHERD30T constructs and selected on gentamicin.

Chromosomal Thoeris integration

For chromosomal insertion of the MRSN390231 Thoeris SIR2 (Pa231) operon at the Tn7 locus in *P. aeruginosa* PAO1(PAO1 Tn7:Thoeris SIR2), the integrating vector pUC18-mini-Tn7T-LAC⁵³ carrying Thoeris operon and the transposase-expressing helper plasmid pTNS3⁵⁴ were used. pUC18-mini-Tn7T-LAC empty vector was used for the creation of the control strain (PAO1 Tn7:empty). The vector was linearized using around-the-world PCR (in positions of KpnI and BamHI sites), treated with DpnI and then purified. The insert was amplified using MRSN390231 overnight culture as a DNA template and joined with linearized pUC18-mini-Tn7T-LAC vector using Hi-Fi DNA Gibson Assembly (NEB) according to the manufacturer's protocol. The resulting plasmids were used to transform *E. coli* DH5α. All plasmid constructs were verified by whole-plasmid sequencing. *P. aeruginosa* PAO1 cells were electroporated with pUC18-mini-Tn7T-LAC and pTNS3 and selected on gentamicin-containing plates. Potential integrants were screened by colony PCR with primers PTn7R and PgImS-down⁵³. Electrocompetent cell preparations, transformations, integrations, selections, plasmid curing and FLP-recombinase-mediated marker excision with pFLP were performed as described previously⁵³.

Phage growth

The phages F10, phiKZ and JBD67(Δacb2) were grown on *P. aeruginosa* PAO1, which lacks CBASS and Thoeris systems. Phage PaMx41(Δacb2) was grown on *P. aeruginosa* BWHPSA011 (Pa011) ΔCBASS strain. For phage propagation 100 µl of *P. aeruginosa* overnight cultures was infected with 10 µl of low-titre phage lysate (>10⁴⁻⁷ plaque-forming units (PFU) per ml) and then mixed with 3 ml of 0.35% top agar 10 mM MgSO₄ for plating on the LB solid agar (20 ml LB agar with 10 mM MgSO₄). After incubating at 37 °C overnight, 2.5 ml SM phage buffer was added on the solid agar lawn and then incubated for 10 min at room temperature. The whole-cell lysate was collected, a 10% volume of chloroform was added and the tubes were left for 20 min at room temperature with gentle shaking, followed by centrifugation at maximum speed for 3 min 4 °C to remove cell debris. The supernatant phage lysate was stored at 4 °C for downstream assays.

Phage gene knockout

Deletion of *orf184* in the phiKZ genome was performed using the protocol developed previously³⁷.

In brief, 100 µl of overnight culture of *P. aeruginosa* PAO1 strain bearing the editing plasmid for homologous recombination (with homologous arms of 600 bp with insertion of *acrVIA1* gene in place of phiKZ *orf184*) was infected with 10 µl of phiKZ WT phage (10⁶ PFU per ml), mixed with 4 ml of 0.35% top agar 10 mM MgSO₄ for plating on the LB solid agar (20 ml LB agar with 10 mM MgSO₄). After incubating 30 °C overnight, the phage was collected from plates. The lysates were plated on PAO1 strains bearing CRISPR–Cas13a system with crRNA targeting phiKZ genome to screen for recombinants. Individual phage plaques were picked from top agar and purified for three more rounds. The deletion of the gene was confirmed by PCR with primers flanking the deletion region and sequencing of the corresponding PCR product.

Plaque assays

Plaque assays were conducted at 37 °C (30 °C for phiKZ phage) with solid LB agar plates supplemented with 10 mM MgSO₄, 50 µg ml⁻¹

gentamicin, 0.2–0.3% L-arabinose and 0.3 mM IPTG for PAO1 strains with CBASS or Thoeris operon chromosomal integration, and the same conditions except without IPTG for the native CBASS and Thoeris strains. A total of 100 µl of overnight bacterial culture was mixed with top agar (0.35% agar in LB) and plated. Phage lysates were diluted tenfold, then 2.5 µl spots were applied to the top agar after it had been poured and solidified. The plates were incubated overnight at 37 °C (30 °C for phiKZ phage).

Bioinformatic analysis of CD-NTases

CD-NTases were identified within the bacterial hosts relevant for each Tad protein by using a protein BLAST (BLASTp) search. A previously curated list of CD-NTase sequences²² was queried against *Clostridium* (taxid: 1485), *Clostridioides* (taxid: 1870884), *Bacteroides* (taxid: 816), *Sphingobacterium* (taxid: 28453) and *B. cereus* group (taxid: 86661). There is only one CD-NTase record for *Salegentibacter* (taxid: 143222) and zero for *Colidextribacter* (taxid: 1980681), so a list of CD-NTase across bacterial taxonomies was used from a previous study²². These lists of CD-NTases were queried against the NCBI non-redundant protein database of each respective bacterial genus as indicated above. A genus-level analysis was chosen due to the diversity of CD-NTase sequences associated with the different clades, which are known or predicted to produce specific cyclic oligonucleotides. Hits from the BLASTp search with >24.5% amino acid identity, >50% coverage, and an *E* value of <0.0005 were identified as CD-NTases. Two or more CD-NTases per CD-NTase clade per bacterial genus were queried using Defense Finder^{28,55}, which revealed that all CD-NTases identified are a part of a CBASS system. A total of 183 CD-NTase hits were identified in *Clostridium* and nine hits were identified in *Clostridioides*, so their results were combined as 202 total hits in Extended Data Fig. 1. A total of 107 hits were identified in *Bacteroides*, 71 were identified in *Sphingobacterium* and 270 were identified in *B. cereus* group. Six hits were found for *Salegentibacter* and zero hits were found for *Colidextribacter*.

Phylogenetic tree analysis

Tad1 and Tad2 homologues were identified using SBSTad1 (NCBI: P0DW57) and SPO1Tad2 (NCBI: YP_002300464.1), respectively, as query proteins to seed a position-specific iterative blast (PSI-BLAST) search of the NCBI non-redundant protein database. Three rounds of PSI-BLAST searches were performed with a max target sequence of 5,000 and *E*-value cut-off of 0.005 for inclusion in the next search round, BLOSUM62 scoring matrix, gap costs settings existence 11 and extension 1 and using conditional compositional score matrix adjustment. Hits from the third search round of PSI-BLAST with >70% coverage, *E* value of <0.0005 and length less than 190 amino acids (for Tad1) and length 70–120 amino acids (for Tad2) were clustered using MMSeq⁵⁶ to remove protein redundancies (minimum sequence identity = 0.9 for Tad1 and 0.8 for Tad2, minimum alignment coverage = 0.9), which resulted in 410 and 667 representative Tad1 and, correspondingly, Tad2 homologue sequences. MAFFT (FFT-NS-I iterative refinement method)⁵⁷ was used to create protein alignment. Manual analysis of the MAFFT protein alignment was performed to ensure the presence of at least one of the cyclic oligonucleotide-binding site regions and to remove non-relevant sequences. The final aligned 385 and 568 sequences (Tad1 and Tad2, respectively) were used to construct a phylogenetic tree using FastTree⁵⁸ and then visualized and annotated in iTOL⁵⁹.

Statistics and Reproducibility

All PAGE assays and histogram analyses in this Article are from three independent replicate experiments to ensure reproducibility. Statistics were calculated in GraphPad Prism by applying the built-in one-way ANOVA and Dunnett's multiple comparison test. ****P*<0.0001, ***P*=0.0012; NS, not significant.

Article

Reporting summary

Further information on research design is available in the Nature Portfolio Reporting Summary linked to this article.

Data availability

The coordinate and structure factors reported in this paper have been deposited at the PDB: 8KBB (apo *CmTad1*), 8KBC (*CmTad1-cA₃*), 8KBD (*CmTad1-cAAG*), 8KBE (*CbTad1-1',3'-gcADPR*), 8KBF (*CbTad1-1',3'-gcADPR-cA₃*), 8KBG (*CbTad1-2',3'-cGAMP*), 8KBH (*CbTad1-2',3'-cGAMP-cA₃*), 8KBI (apo *HgmTad2*), 8KBJ (*HgmTad2-1'',2'-gcADPR*), 8KBK (*HgmTad2-1'',2'-gcADPR-cGG*), 8KBL (*HgmTad2-1''-3'-gcADPR-cGG*), 8KBM (*HgmTad2-cGG*), 8WJC (*HgmTad2-3',3'-cGAMP*), 8WJD (*SptTad2-cGG*) and 8WJE (apo *SPO1 Tad2*). All other data are available in the Article, Extended Data Figs. 1–11, Extended Data Table 1 and the Supplementary Information. Source data are provided with this paper.

Code availability

This paper does not report original code.

48. Otwinowski, Z. & Minor, W. Processing of X-ray diffraction data collected in oscillation mode. *Methods Enzymol.* **276**, 307–326 (1997).
49. Jumper, J. et al. Highly accurate protein structure prediction with AlphaFold. *Nature* **596**, 583–589 (2021).
50. Adams, P. D., Grosse-Kunstleve, R. W., Hung, L. W., Ioerger, T. R. & Terwilliger, T. C. PHENIX: building new software for automated crystallographic structure determination. *Acta Crystallogr. D* **58**, 1948–1954 (2002).
51. Emsley, P., Lohkamp, B., Scott, W. & Cowtan, K. Features and development of Coot. *Acta Crystallogr. D* **66**, 486–501 (2010).
52. Qiu, D., Damron, F. H., Mima, T., Schweizer, H. P. & Yu, H. D. PBAD-based shuttle vectors for functional analysis of toxic and highly regulated genes in *Pseudomonas* and *Burkholderia* spp. and other bacteria. *Appl. Environ. Microbiol.* **74**, 7422–7426 (2008).
53. Choi, K. H. & Schweizer, H. P. Mini-Tn7 insertion in bacteria with single attTn7 sites: example *Pseudomonas aeruginosa*. *Nat. Protoc.* **1**, 153–161 (2006).
54. Choi, K. H. et al. Genetic tools for select-agent-compliant manipulation of *Burkholderia pseudomallei*. *Appl. Environ. Microbiol.* **74**, 1064–1075 (2008).
55. Abby, S. S., Néron, B., Ménager, H., Touchon, M. & Rocha, E. P. MacSyFinder: a program to mine genomes for molecular systems with an application to CRISPR-Cas systems. *PLoS ONE* **9**, e110726 (2014).
56. Steinegger, M. & Söding, J. MMseqs2 enables sensitive protein sequence searching for the analysis of massive data sets. *Nat. Biotechnol.* **35**, 1026–1028 (2017).
57. Katoh, K., Rozewicki, J. & Yamada, K. D. MAFFT online service: multiple sequence alignment, interactive sequence choice and visualization. *Brief. Bioinform.* **20**, 1160–1166 (2019).
58. Price, M. N., Dehal, P. S. & Arkin, A. P. FastTree 2—approximately maximum-likelihood trees for large alignments. *PLoS ONE* **5**, e9490 (2010).
59. Letunic, I. & Bork, P. Interactive Tree Of Life (iTOL) v5: an online tool for phylogenetic tree display and annotation. *Nucleic Acids Res.* **49**, W293–w296 (2021).

Acknowledgements We thank the staff at beamlines BL02U1 and BL19U1 of the Shanghai Synchrotron Radiation Facility for their assistance with data collection; the staff at the Tsinghua University Branch of China National Center for Protein Sciences Beijing and S. Fan for providing facility support for X-ray diffraction of the crystal samples; and Y. Chen, Z. Yang and B. Zhou at the Institute of Biophysics, Chinese Academy of Sciences for technical help with ITC and SPR experiments. Y.F. is supported by National key research and development program of China (2022YFC3401500 and 2022YFC2104800), the National Natural Science Foundation of China (32371329 and 32171274), Beijing Nova Program (20220484160) and the Fundamental Research Funds for the Central Universities (QNTD2023-01). E.H. is supported by the National Science Foundation Graduate Research Fellowship Program (grant no. 2038436). J.B.-D. is supported by the US National Institutes of Health (R21AI168811 supported CBASS/Therois experiments; R01GM127489 supported CRISPR-Cas9 experiments), the Vallee Foundation and the Searle Scholarship. Any opinions, findings and conclusions or recommendations expressed in this Article are those of the authors and do not necessarily reflect the views of the National Science Foundation.

Author contributions Y.F. and J.B.-D. conceived and supervised the project and designed experiments. D.L., W.X., Y.W., X.L., Z.G., X.Z. and X.C. purified the proteins, grew and optimized the crystals, collected the diffraction data, and performed in vitro activity analysis and binding assays. Y.X. solved the crystal structures with the help of Y.F. and Y.Z.; I.F. performed in vivo phage experiments, strain engineering and Tad1/Tad2 protein bioinformatics. J.R. performed HPLC assays. E.H. performed cyclase bioinformatics. Y.F. wrote the original manuscript. J.B.-D., Y.F., I.F. and E.H. revised the manuscript.

Competing interests J.B.-D. is a scientific advisory board member of SNIPR Biome and Excision Biotherapeutics, a consultant to LeapFrog Bio and BiomX, and a scientific advisory board member and co-founder of Acrigen Biosciences and ePfective Therapeutics. The J.B.-D. laboratory received prior research support from Felix Biotechnology.

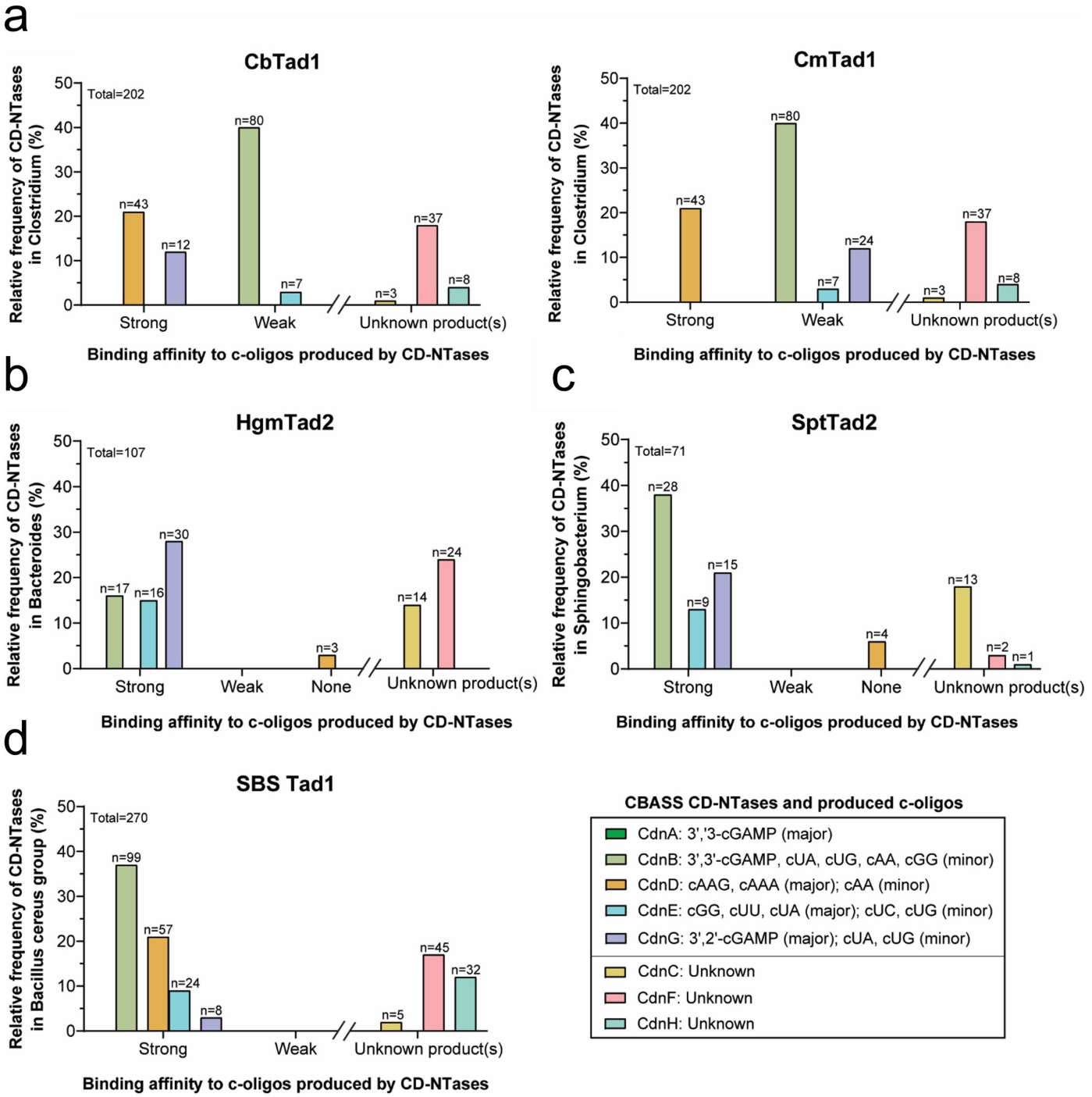
Additional information

Supplementary information The online version contains supplementary material available at <https://doi.org/10.1038/s41586-024-08122-4>.

Correspondence and requests for materials should be addressed to Joseph Bondy-Denomy or Yue Feng.

Peer review information *Nature* thanks Philip Kranzusch and the other, anonymous, reviewer(s) for their contribution to the peer review of this work. Peer reviewer reports are available.

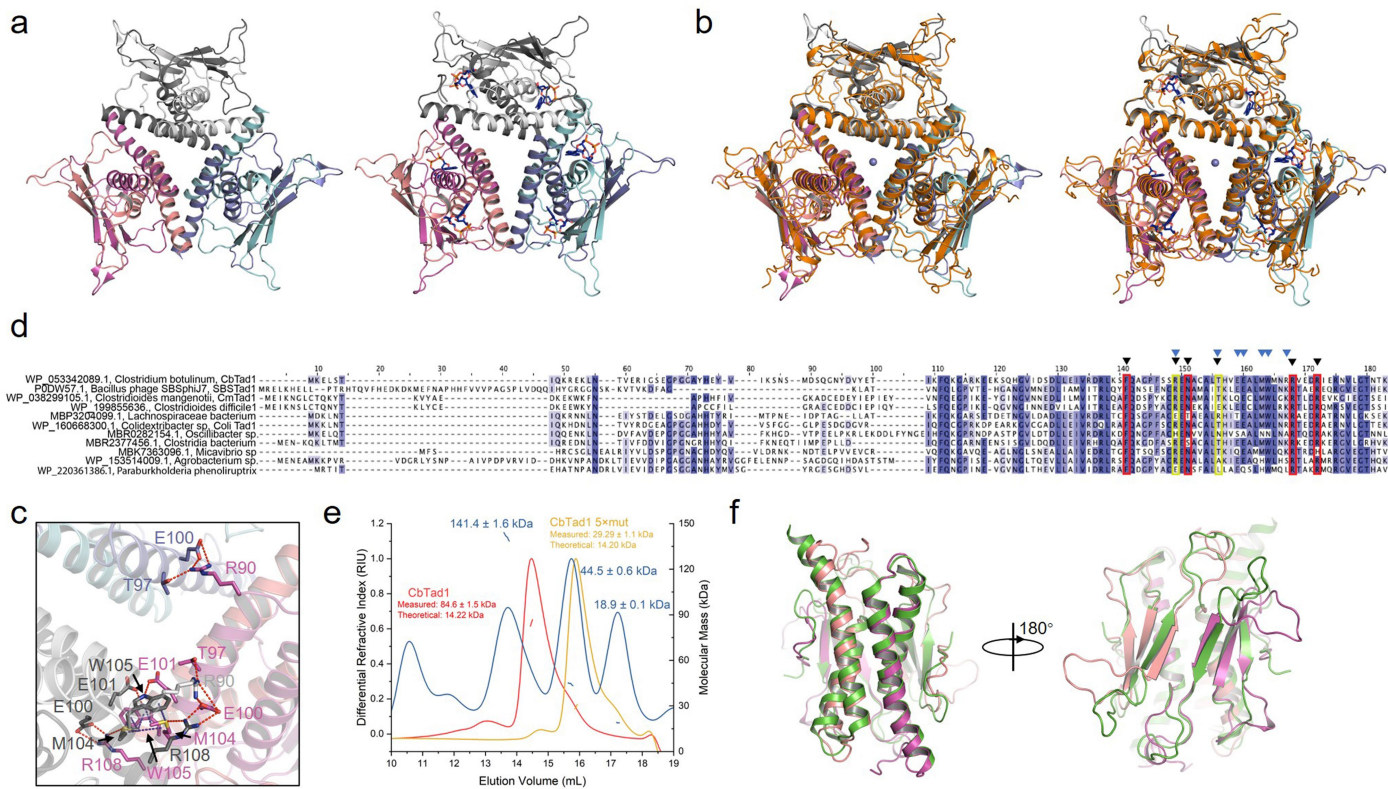
Reprints and permissions information is available at <http://www.nature.com/reprints>.



Extended Data Fig. 1 | Bacterial hosts that Tad-encoding phage likely infect contain multiple CBASS CD-NTases that produce cyclic oligonucleotides. Bacteria from the genus (a) *Clostridium*, (b) *Bacteroides*, (c) *Sphingobacterium*, and (d) *Bacillus cereus* group contain CBASS CD-NTases that produce cyclic oligonucleotides (c-oligos) with strong, weak, or no binding affinity to the Tad proteins tested in this study. The relative frequency of CD-NTases is quantified

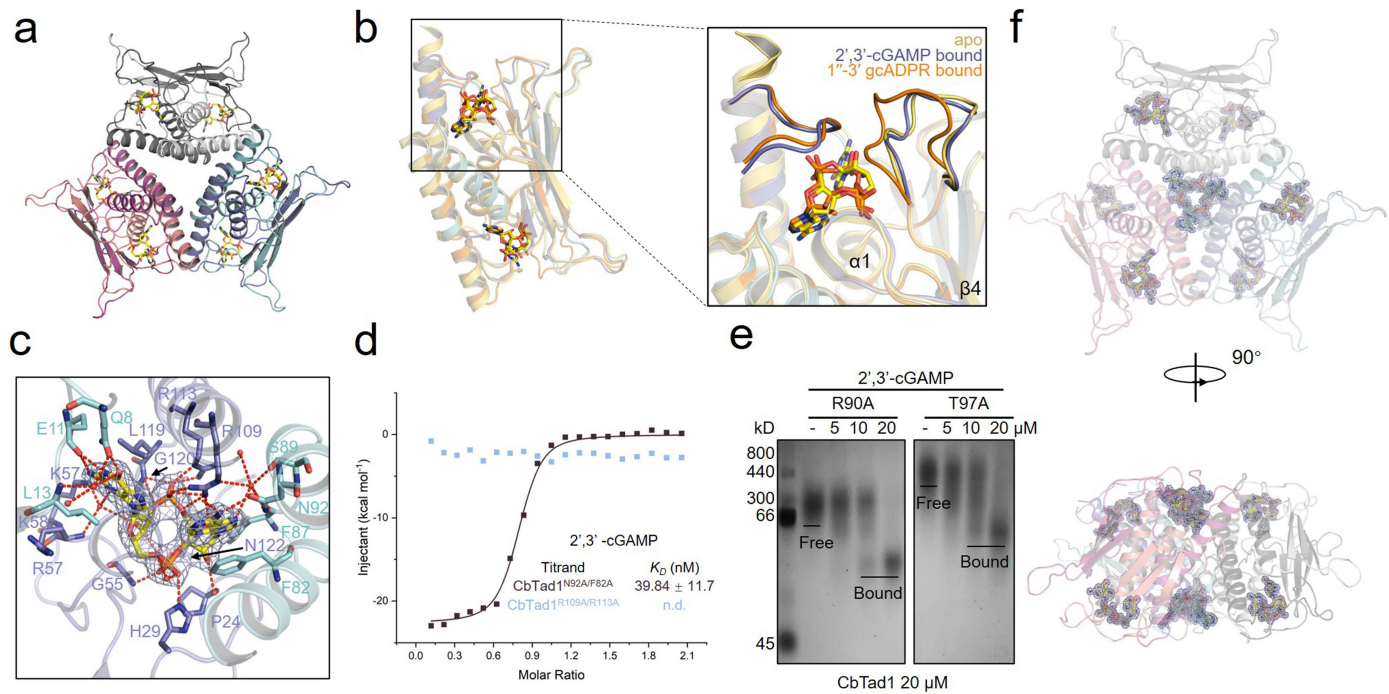
as the number of CD-NTase from a specific clade divided by the total number of CD-NTases identified using the NCBI blastp (see Methods for details). The legend indicates the c-oligos that are known or predicted to be produced by the indicated CBASS CD-NTases (Whiteley et al.²²; Ye et al.³⁴; Morehouse et al.⁴⁰; Fatma et al.²³). CD-NTases with currently unknown nucleotide products are indicated in the legend and the graphs.

Article



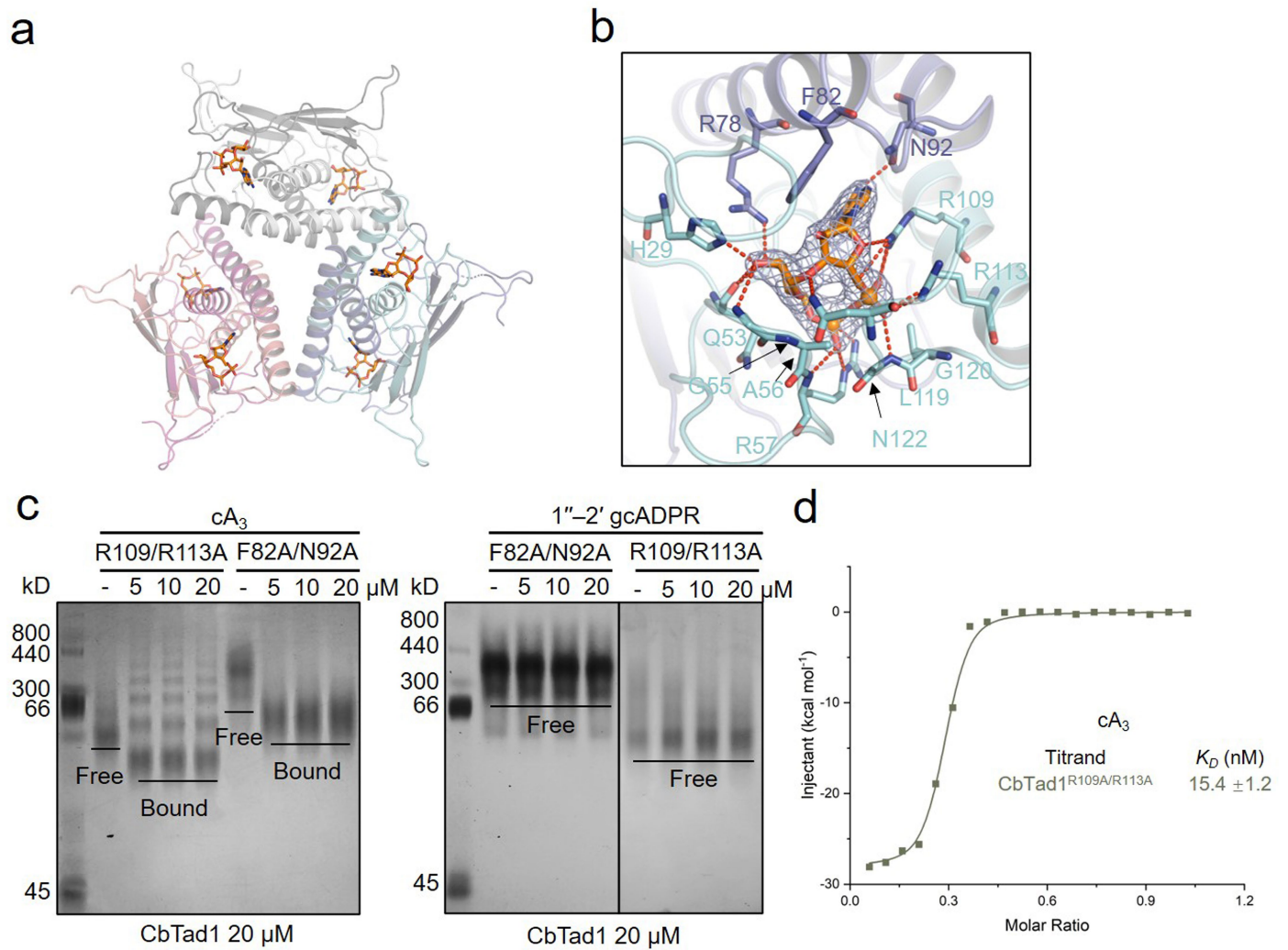
Extended Data Fig. 2 | Structural comparison between CbTad1 and CmTad1.
a, The hexameric form of CbTad1 are shown in cartoon model. Left: CbTad1 (PDB code: 7UAV). Right: CbTad1-1'-2' gcADPR (PDB code: 7UAW). **b**, Structural comparison between CbTad1 and CmTad1 hexamers. Left: structural comparison between apo CbTad1 (coloured as in a) and apo CmTad1 (coloured orange). Right: structural comparison between CbTad1-1'-2' gcADPR (coloured as in a) and apo CmTad1 (coloured orange). **c**, Detailed binding in the hexamer interface of CbTad1. Residues involved in hexamer formation are shown as sticks. Red dashed lines represent polar interactions. **d**, Sequence alignment between Tad1 homologues. The cyclic trinucleotide (CTN) and cyclic

dinucleotides (CDN)/gcADPR binding sites are marked in yellow and red, respectively. Representative sequences were intentionally selected to show CTN/CTN binding site mutations. Residues involved in hexamer formation are marked with blue triangles. **e**, SLS studies of purified CbTad1 and its E100A/E101A/M104A/W105A/R108A mutant. Calculated molecular weight is shown above the peaks. Profile of the molecular standard sample is coloured in dark blue. **f**, Structural comparison between the dimer form of CbTad1 and CmTad1. Apo CbTad1 (PDB code: 7UAV) is coloured green. Apo CmTad1 is coloured in pink and magenta for the two protomers.



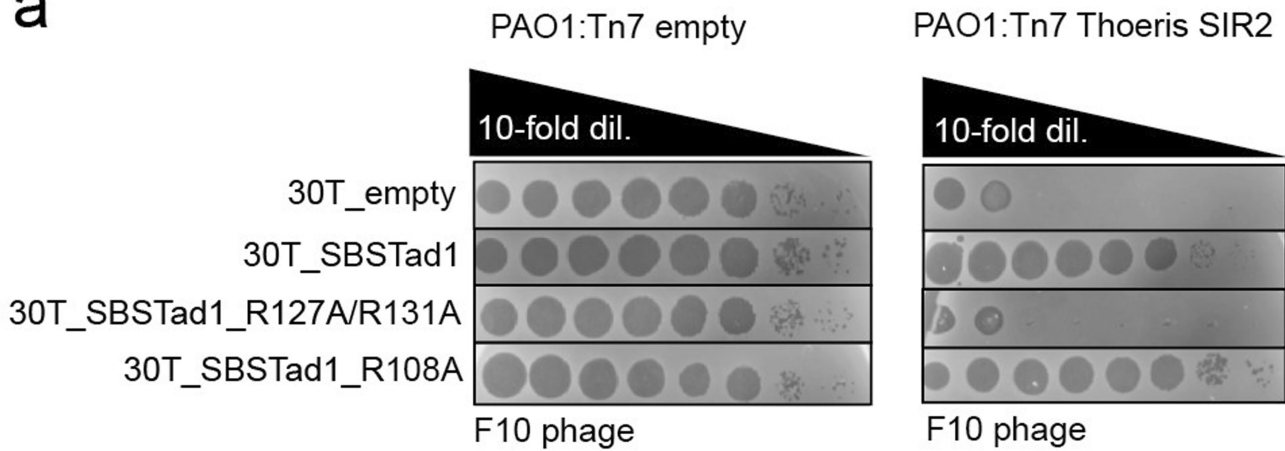
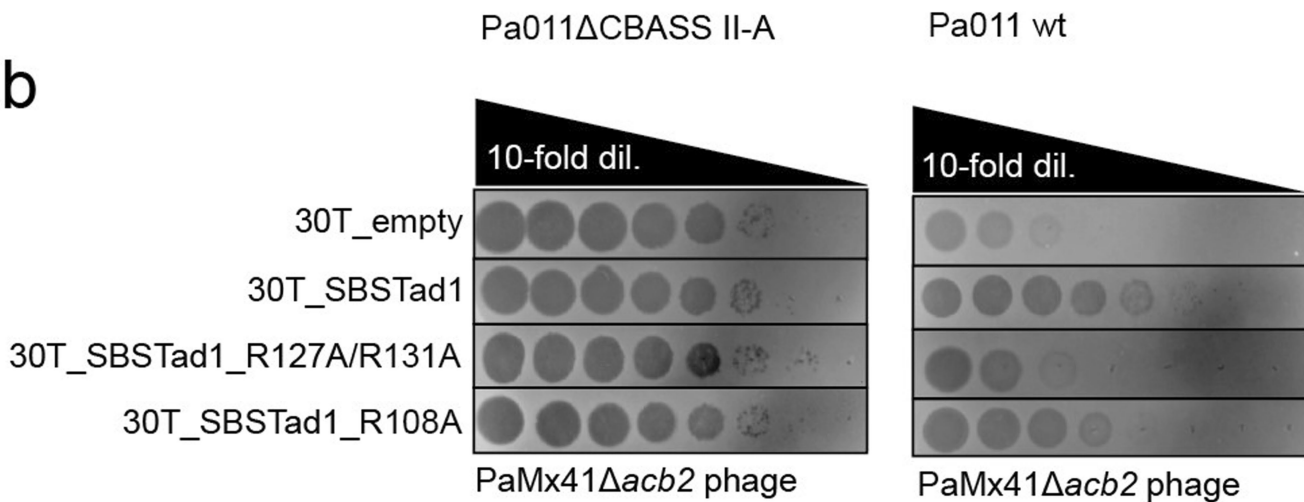
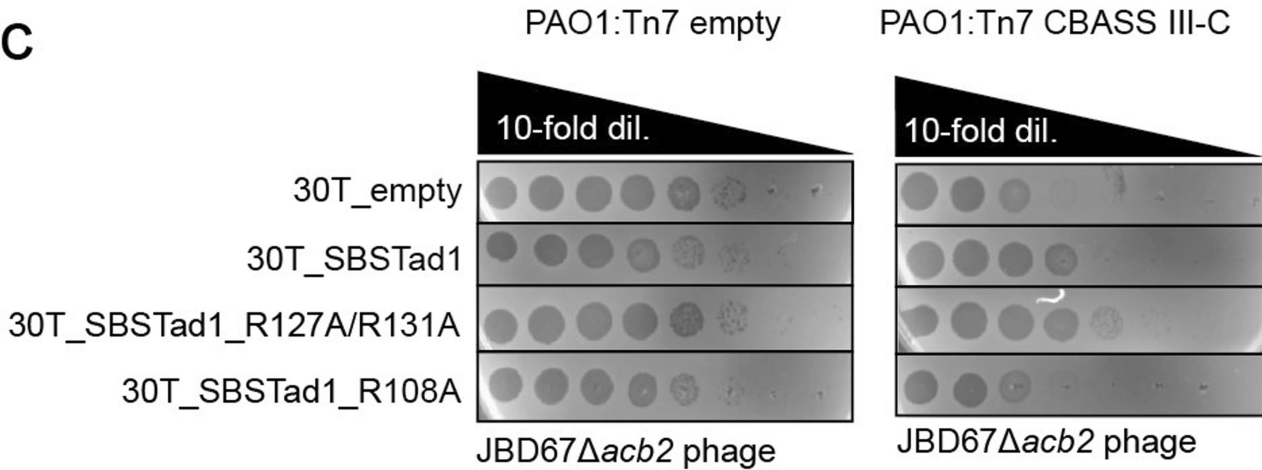
Extended Data Fig. 3 | Tad1 binds to 2',3'-/3',2'-cGAMP using the same binding pocket as gcADPR molecules. **a**, Overall structure of CbTad1 hexamer bound to 2',3'-cGAMP, which is shown as yellow sticks. **b**, Structural superimposition of apo, 1''-3' gcADPR-bound and 2',3'-cGAMP-bound CbTad1 protein. 1''-3' gcADPR and 2',3'-cGAMP are shown as orange and yellow sticks, respectively. The two loops that undergo conformational changes upon ligand binding are highlighted. **c**, Detailed binding between CbTad1 and 2',3'-cGAMP. Residues involved in 2',3'-cGAMP binding are shown as sticks. Red dashed lines represent polar interactions. 2Fo-Fc electron density of 2',3'-cGAMP within one

binding pocket is shown and contoured at 1σ . **d**, ITC assays to test binding of 2',3'-cGAMP to CbTad1 mutants. Representative binding curves and binding affinities are shown. The K_D values are mean \pm s.d. ($n = 3$ independent experiments). Raw data for these curves are shown in Supplementary Fig. 3. **e**, Native PAGE showed the binding of CbTad1 and its mutants to 2',3'-cGAMP. For gel source data, see Supplementary Fig. 1. **f**, Overall structure of CmTad1 hexamer complexed with cA3 and 2',3'-cGAMP. cA3 and 2',3'-cGAMP are shown as green and yellow sticks, respectively. Two views are shown. 2Fo-Fc electron density of cA3 and 2',3'-cGAMP within CbTad1 hexamer contoured at 1σ .



Extended Data Fig. 4 | Binding of 1''-3'-gcADPR by CbTad1. **a**, Overall structure of CbTad1 hexamer bound to 1''-3' gcADPR, which is shown as orange sticks. **b**, Detailed binding between CbTad1 and 1''-3' gcADPR. Residues involved in 1''-3' gcADPR binding are shown as sticks. Red dashed lines represent polar interactions. 2Fo-Fc electron density of 1''-3' gcADPR within one binding pocket is shown and contoured at 1σ. **c**, Native PAGE showed the

binding of CbTad1 mutants to cA₃ and 1''-2' gcADPR. For gel source date, see Supplementary Fig. 1. **d**, ITC assays to test binding of cA₃ to CbTad1 mutant. Representative binding curves and binding affinities are shown. The K_D values are mean \pm s.d. ($n = 3$ independent experiments). Raw data for these curves are shown in Supplementary Fig. 3.

a**b****c**

Article

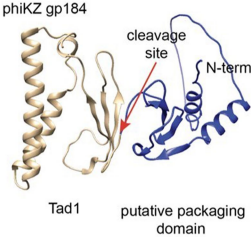
Extended Data Fig. 5 | Mutations in independent nucleotide binding sites of SBS Tad1 disrupt specific inhibitory activities. **a**, Plaque assay to test the activity of SBS Tad1 against Thoeris immunity in vivo. F10 phage was spotted in 10-fold serial dilutions on a lawn of *P. aeruginosa* cells expressing Thoeris operon genes (PAO1:Tn7 Thoeris SIR2), or without Thoeris (PAO1:Tn7 empty), electroporated with pHERD30T plasmids carrying *SBS tad1* (wild type or mutant gene) or empty vector. **b**, Plaque assay to test the activity of SBS Tad1 against CBASS II-A^{GA} immunity in vivo. PaMx41Δ*acb2* was spotted on a lawn of

Pa011 cells with deletion of CBASS operon (Pa011ΔCBASS II-A^{GA}) or Pa011 wild type cells (Pa011 wt), electroporated with pHERD30T plasmids carrying SBS Tad1 (wild type or mutant gene) or empty vector. **c**, Plaque assay to test the activity of SBS Tad1 against CBASS III-C^{AAA} immunity in vivo. JBD67Δ*acb2* phage was spotted in 10-fold serial dilutions on a lawn of *P. aeruginosa* cells expressing Pa278 CBASS operon genes (PAO1:Tn7CBASS III-C^{AAA}), or without the system (PAO1:Tn7 empty), electroporated with pHERD30T plasmids carrying *SBS tad1* (wild type or mutant gene) or empty vector.

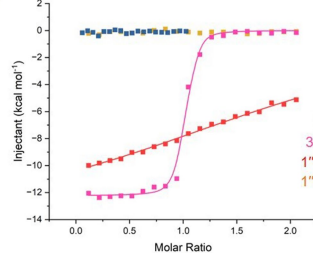
a



b



c



phiKZ Tad1
Syringe
3',3'-cGAMP
1"-3' gcADPR
1"-2' gcADPR
cA3

K_D (nM)

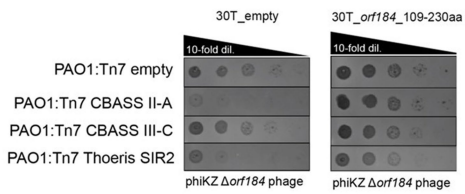
13.4 ± 0.5

7587.3 ± 366.6

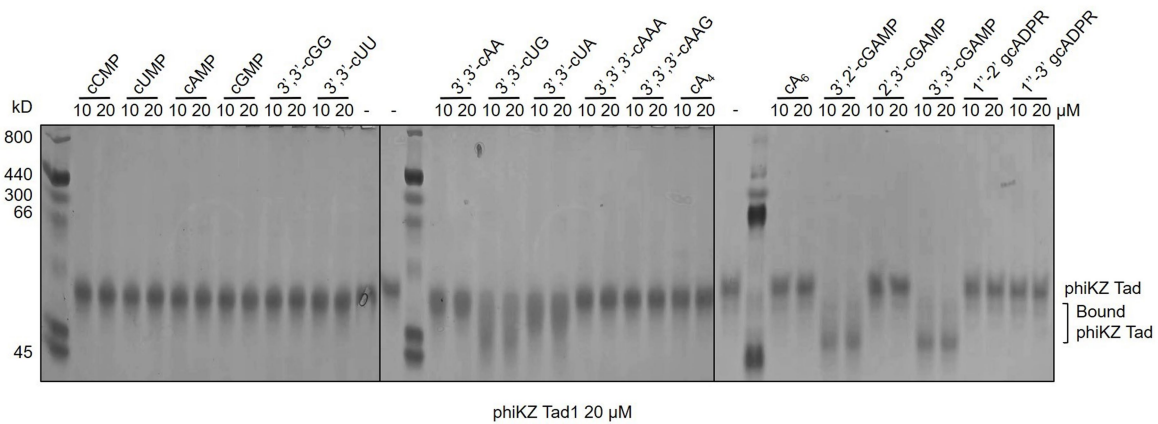
n.d.

n.d.

e



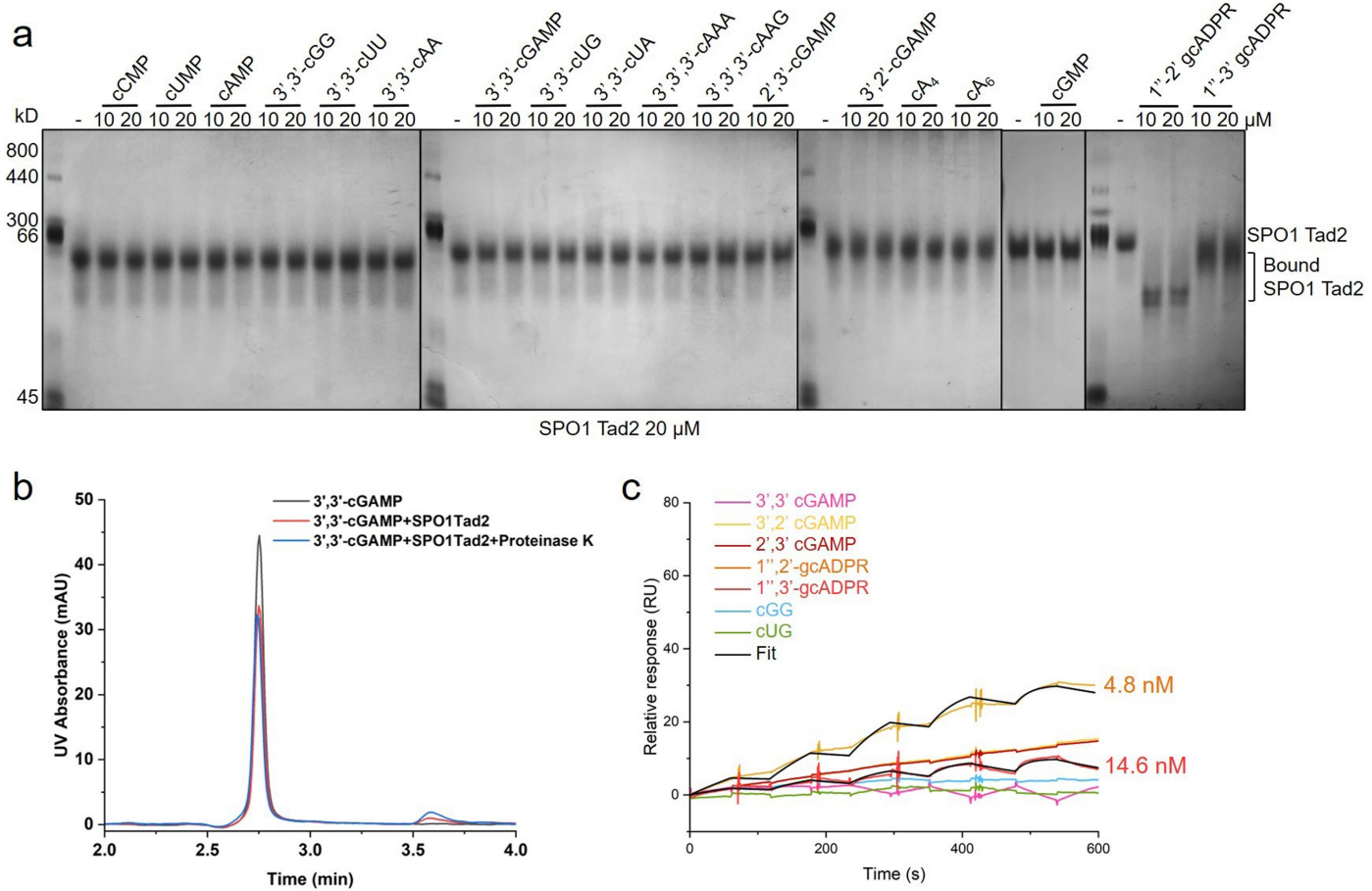
d



Extended Data Fig. 6 | PhiKZ gp184 is Tad1 sponge protein that binds CDN/gcADPR molecules. a, Sequence alignment among phiKZ Tad1 homologues and SBS Tad1. For Tad1 proteins from phiKZ, PA7, phiPA3, Phabio phages the sequences without N-terminal domain (putative packaging domains) were used for alignment. CDN/gcADPR binding sites are shown with red frames, CTN binding sites are shown with yellow frames. Arrows indicate mutations in the binding sites. The enumeration of start and end amino acid positions is shown for phiKZ gp184. b, ColabFold prediction of phiKZ gp184 structure. The Tad1 domain is in gold, and the putative packaging domain is in blue. The protease cleavage site position H109 is indicated with a red arrow. c, ITC assays to test binding of 3',3'-cGAMP, 1",3'- and 1",2'-gcADPR

to phiKZ Tad1. Representative binding curves and binding affinities are shown. The K_D values are mean \pm s.d. ($n = 3$ independent experiments). Raw data for these curves are shown in Supplementary Fig. 9. d, Native PAGE showed the binding of phiKZ Tad1 to cyclic nucleotides and gcADPR molecules. For gel source date, see Supplementary Fig. 1. e, Plaque assay to test the activity of phiKZ gp184 against CBASS II-A^{G4} immunity in vivo. phiKZΔgp184 was spotted on a lawn of *P. aeruginosa* cells expressing Pa278 CBASS operon genes (PAO1:Tn7CBASS III-C^{AAA}), Pa011 CBASS operon genes (PAO1:Tn7CBASS II-G^A), Thoeris SIR2 operon genes (PAO1:Tn7 Thoeris I) or without the system (PAO1:Tn7 empty). Cells were electroporated with pHERD30T plasmids carrying phiKZ gp184 (109–230 amino acids) or empty vector.

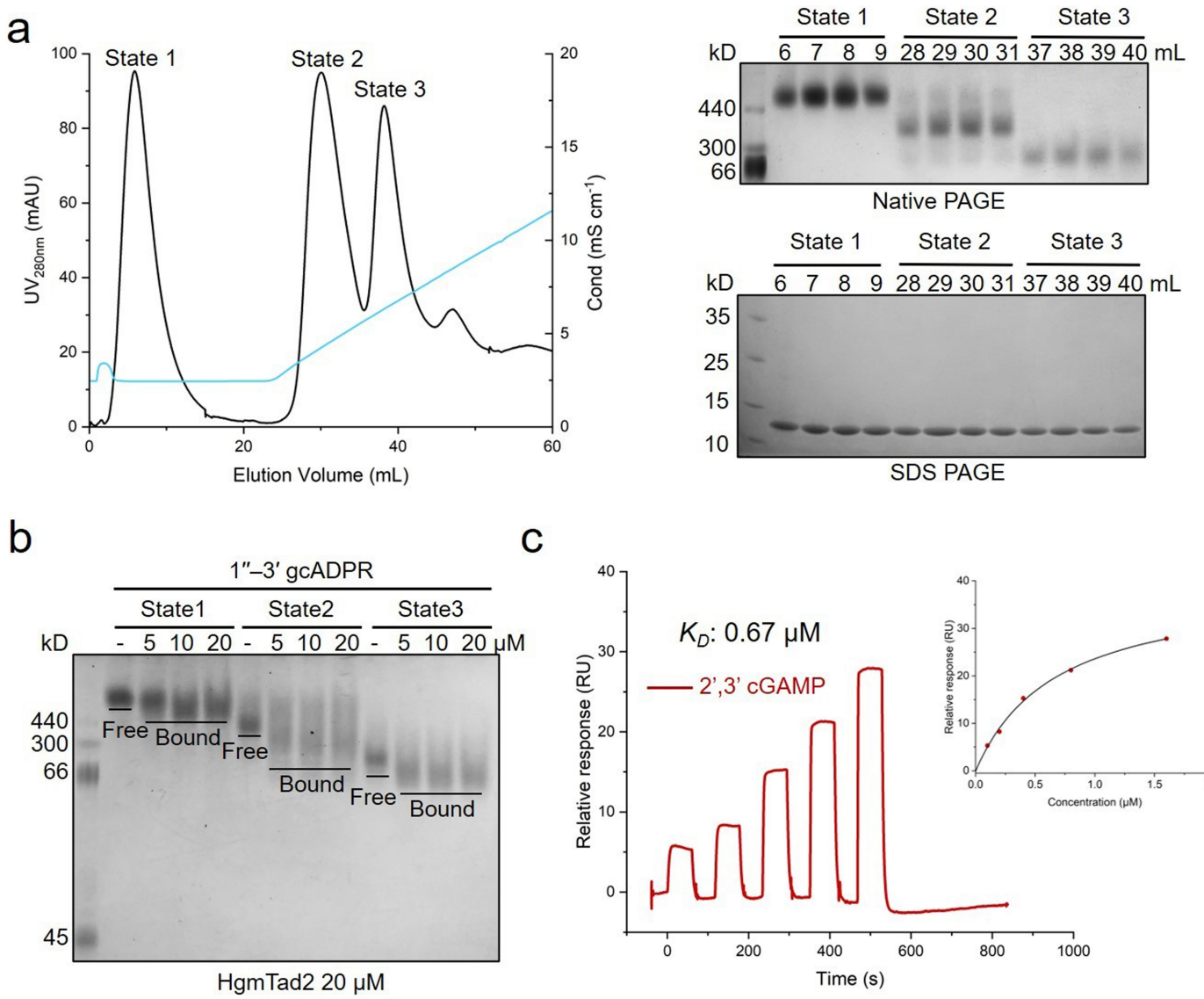
Article



Extended Data Fig. 7 | SPO1 Tad2 does not bind to cyclic dinucleotides.

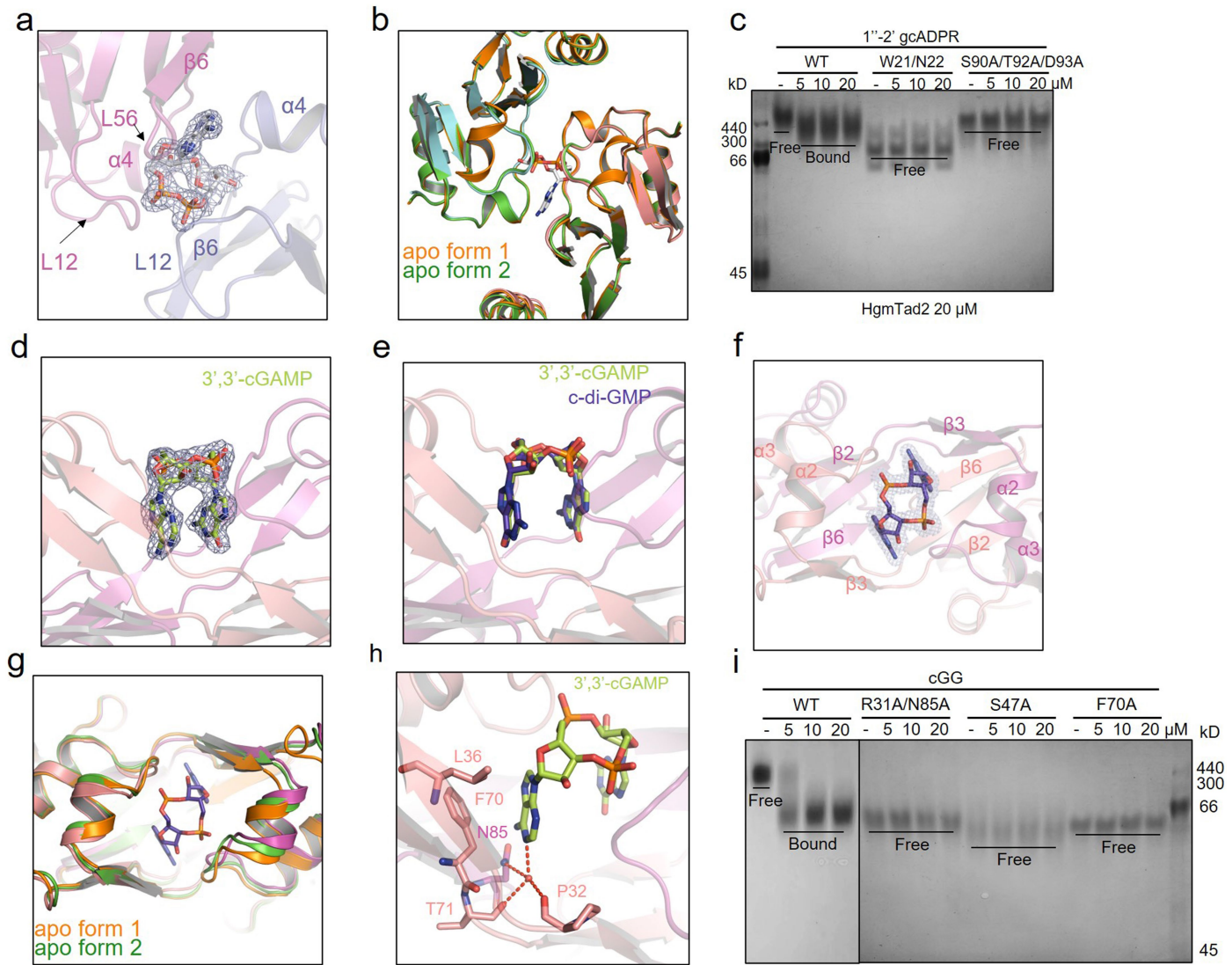
a, Native PAGE showed the binding of SPO1 Tad2 to cyclic nucleotides and gcADPR molecules. For gel source date, see Supplementary Fig. 1. **b**, The ability of SPO1 Tad2 to bind and release 3',3'-cGAMP when treated with proteinase K was analysed by HPLC. 3',3'-cGAMP was used as a control. The remaining

nucleotides after incubation with SPO1 Tad2 was tested. **c**, Overlay of sensograms from surface plasmon resonance (SPR) experiments, used to determine kinetics of SPO1 Tad2 binding to cyclic dinucleotides. Data were fit with a model describing one-site binding for the ligands (black lines).



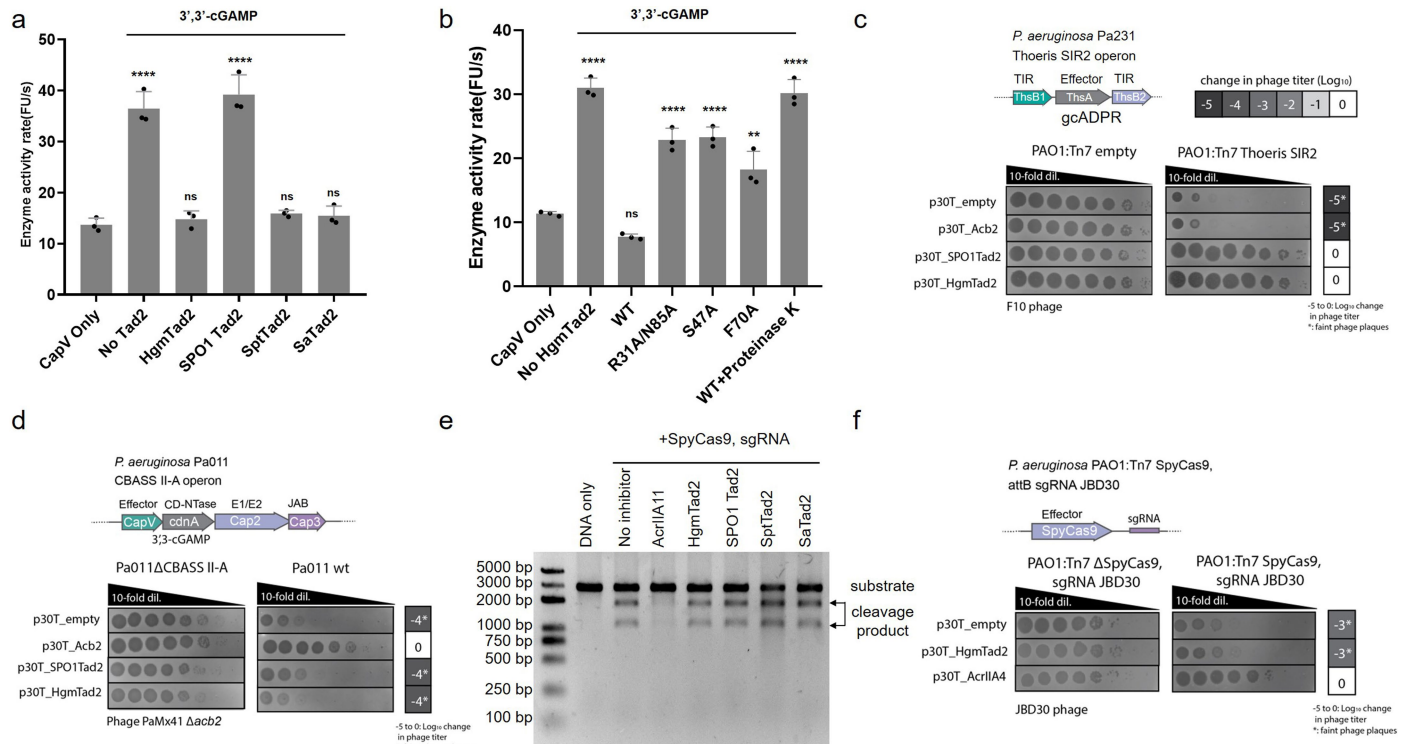
Extended Data Fig. 8 | HgmTad2 binds to cGG and gcADPR molecules.
a, Profile of ion exchange chromatography of HgmTad2 using Resource Q column (1mL, GE Healthcare). Proteins in peaks 1–3 are collected separately and marked as State 1–3. The proteins in three states were then subjected to

native PAGE and SDS-PAGE, respectively. **b**, Native PAGE showed the binding of HgmTad2 in three states to 1'',2' gcADPR. For gel source date of **a** and **b**, see Supplementary Fig. 1. **c**, SPR analysis of HgmTad2 binding to 2',3'-cGAMP. The data was fitted with affinity model and the calculated K_D was shown.



Extended Data Fig. 9 | The binding pockets of 1''-2' gcADPR and cGG. **a**, The binding pocket of 1''-2' gcADPR in the HgmTad2-1''-2' gcADPR structure. 2Fo-Fc electron density of 1''-2' gcADPR is shown and contoured at 1 σ . **b**, Structural superposition among HgmTad2 in the apo form (two types of conformations) and 1''-2' gcADPR-bound form. HgmTad2 in the apo form is coloured orange and green for two types of conformations, respectively. HgmTad2 in the 1''-2' gcADPR-bound form is coloured cyan and pink for the two protomers. **c**, Native PAGE showed the binding of HgmTad2 and its mutants to 1''-2' gcADPR. **d**, The binding pocket of 3',3'-cGAMP in the HgmTad2-3',3'-cGAMP structure. 2Fo-Fc electron density of 3',3'-cGAMP is shown and contoured at 1 σ . **e**, Structural

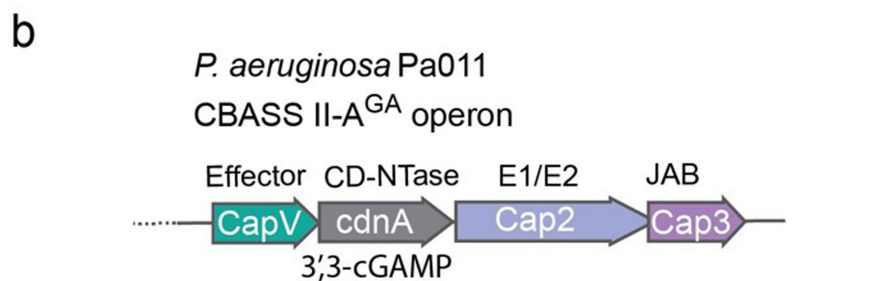
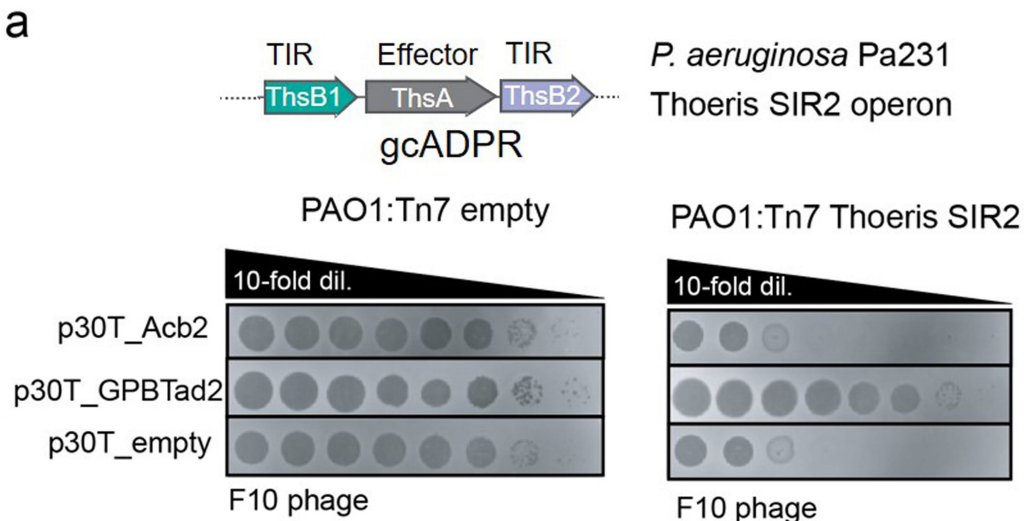
superposition between HgmTad2-3',3'-cGAMP and HgmTad2-cGG. 3',3'-cGAMP and cGG bind at the same position. **f**, The binding pocket of cGG in the HgmTad2-cGG structure. 2Fo-Fc electron density of cGG is shown and contoured at 1 σ . **g**, Structural superposition among HgmTad2 in the apo form (two types of conformations) and cGG-bound form. HgmTad2 in the apo form is coloured orange and green for two types of conformations, respectively. HgmTad2 in the cGG-bound form is coloured light magenta and pink for the two protomers. **h**, Closer view of the binding of the adenine base of 3',3'-cGAMP in the binding pocket of HgmTad2. **i**, Native PAGE showed the binding of HgmTad2 mutants to 3',3'-cGAMP. For gel source date of **c** and **i**, see Supplementary Fig. 1.



Extended Data Fig. 10 | HgmTad2 has anti-Thoeris activity, but lacks anti-CBASS and anti-CRISPR-Cas activity in vivo. a,b CapV enzyme activity in the presence of 3',3'-cGAMP and resorufin butyrate. The enzyme activity rate was measured by the accumulation rate of fluorescence units (FU) per second. HgmTad2 (8 μ M) was incubated with 3',3'-cGAMP (0.8 μ M) for 10 min and then proteinase K (0.708 mg/mL) was added to release the nucleotide from the HgmTad2 protein. Filtered nucleotide products were used for the CapV activity assay. Data are mean \pm SD (n = 3 independent experiments). P-value: ****p < 0.0001. **p = 0.0012. **c**, Plaque assays with 10-fold dilutions of phage F10

to test the activity of SPO1Tad2 and HgmTad2 against SIR2 containing Thoeris system in vivo. Acb2/Tad2 expressed from p30T plasmid. **d**, Plaque assays with 10-fold dilutions of PaMx41 Δ acb2 to test the activity of SPO1Tad2 and HgmTad2 against Type II-A $^{\alpha}$ CBASS in vivo. **e**, In vitro DNA cleavage with SpyCas9 (100 nM), sgRNA (150 nM), substrate DNA (10 nM), and AcrIIA11/Tad2 proteins (10 μ M). Cleavage produce presence indicates no inhibitor activity. For gel source date, see Supplementary Fig. 1. **f**, Plaque assays with 10-fold dilutions of phage JBD30 to test the activity of HgmTad2 against CRISPR-Cas9 system in *P. aeruginosa*.

Article



Extended Data Fig. 11 | GPBTad2 is active against Thoeris SIR2 and CBASS II-A^{GA} in vivo. **a**, Plaque assays to test the activity of GPBTad2 against SIR2 containing Thoeris system in vivo. Organization of *P. aeruginosa* Pa231 Thoeris operon shown. F10 phage was spotted in 10-fold serial dilutions on a lawn of *P. aeruginosa* cells (PAO1) expressing Pa231 Thoeris operon genes (PAO1:Tn7 Thoeris SIR2), or cells without the system (PAO1:Tn7 empty), electroporated with pHERD30T plasmids carrying Acb2 and GPBTad2 genes or empty vector.

b, Plaque assays to test the activity of GPBTad2 against Type II-A^{GA} CBASS in vivo. Organization of the *P. aeruginosa* Pa011 CBASS II-A^{GA} operon shown. PaMx41Δacb2 was spotted in 10-fold serial dilutions on a lawn of Pa011 cells with deletion of CBASS operon (Pa011ΔCBASS II-A) or Pa011 wild type cells (Pa011 wt), electroporated with pHERD30T plasmids carrying Acb2 and GPBTad2 genes or empty vector.

Extended Data Table 1 | Data collection and refinement statistics

	apo-CmTad1	CmTad1-cA ₃	CmTad1-cAAG	CbTad1-1",3'-gcADPR	CbTad1-1",3'-gcADPR-cA ₃	CbTad1-2",3'-cGAMP-cA ₃	CbTad1-2",3'-cGAMP	apo-HgmTa d2	HgmTa d2-1",2'-gcADPR	HgmTa d2-1",2'-gcADPR-cGG	HgmTa d2-1"-3' gcADPR-cGG	HgmTa d2-3",3'-cGAMP	SptTad2-cGG	apo-SPO1 Tad2	
Data collection															
Space group	P 2 ₁ 2 ₁ 2 ₁	P 2 ₁ 2 ₁ 2 ₁	P 2 ₁ 2 ₁ 2 ₁	P 2 ₁ 3	P 2 ₁ 3	P 2 ₁	C 2	P 3 ₂ 21	P 4 ₂ 2 ₁ 2	C 2	P 4 ₂ 2 ₂	C 222	P 2 ₁	P 6422	C 2
Cell dimensions															
<i>a, b, c</i> (Å)	138.8	138.9	138.7	101.1	101.3	71.9	140.7	91.0	101.8	104.3	63.7	88.1	50.2	61.6	111.1
	144.5	145.7	145.1	101.1	101.3	66.0	81.2	91.0	101.8	57.7	63.7	89.8	81.6	61.6	69.1
	150.1	150.8	150.0	101.1	101.3	89.4	128.6	99.1	92.3	92.5	63.2	63.2	50.4	97.5	92.2
α, β, γ (°)	90.0	90.0	90.0	90.0	90.0	90.0	90.0	90.0	90.0	90.0	90.0	90.0	90.0	90.0	90.0
	90.0	90.0	90.0	90.0	90.0	90.0	90.0	90.0	90.0	121.7	90.0	90.0	102.3	90.0	95.9
	90.0	90.0	90.0	90.0	90.0	90.0	90.0	90.0	90.0	90.0	90.0	90.0	90.0	120.0	90.0
Resolution (Å)	41.13-	44.14-	50.00-	31.97-	32.02-	31.47-	38.84-	19.33-	44.58-	26.97-	31.86-	19.77-	31.40-	48.76-	35.19-
	2.56	2.80	3.15	2.16	2.31	2.37	1.54	1.70	2.10	2.28	1.98	1.38	2.11	1.71	2.27
	(2.65-	(2.91-	(3.20-	(2.24-	(2.39-	(2.46-	(1.60-	(1.76-	(2.18-	(2.36-	(2.05-	(1.45-	(2.16-	(1.75-	(2.33-
R_{sym} or R_{merge}	0.241	0.218	0.199	0.070	0.134	0.161	0.199	0.277	0.234	0.093	0.211	0.107	0.197	0.092	0.170
	(2.489)	(2.143)	(133.5)	(1.232)	(2.305)	(1.400)	(1.140)	(1.862)	(2.055)	(1.211)	(2.161)	(1.687)	(1.259)	(2.369)	(2.055)
$I/\sigma I$	10.1	9.4	8.88	31.3	22.0	10.2	5.8	7.8	15.7	11.5	18.6	15.0	8.5	25.8	8.9
	(1.1)	(1.4)	(1.0)	(2.3)	(2.3)	(1.8)	(1.6)	(2.6)	(5.8)	(1.7)	(8.1)	(2.0)	(2.0)	(2.1)	(1.6)
Completeness (%)	100	100	99.2	100	100	99.9	100	100	100	98.2	100	97.9	99.7	99.2	99.3
	(100)	(100)	(97.8)	(100)	(100)	(100)	(99.9)	(100)	(100)	(97.2)	(100)	(95.8)	(99.7)	(99.7)	(98.5)
Redundancy	12.9	13.1	5.0	35.1	40.0	6.8	6.1	39.9	25.3	6.8	24.3	26.4	6.5	35.3	6.6
	(12.8)	(13.7)	(4.1)	(17.8)	(41.1)	(7.1)	(4.8)	(40.0)	(24.8)	(6.3)	(26.0)	(27.6)	(6.5)	(32.4)	(6.8)
Refinement															
Resolution (Å)	41.13-	44.14-	34.76-	31.97-	32.02-	31.47-	38.84-	19.33-	44.58-	26.97-	31.86-	19.77-	31.36-	30.77-	32.51-
	2.56	2.80	3.15	2.16	2.31	2.37	1.54	1.70	2.10	2.28	1.98	1.38	2.11	1.71	2.27
	(2.65-	(2.91-	(3.26-	(2.24-	(2.39-	(2.46-	(1.60-	(1.76-	(2.18-	(2.36-	(2.05-	(1.43-	(2.19-	(1.77-	(2.35-
$R_{\text{work}} / R_{\text{free}}$	0.241	0.218	0.199	0.070	0.134	0.161	0.199	0.277	0.234	0.093	0.211	0.107	0.197	0.092	0.170
	(2.489)	(2.143)	(133.5)	(1.232)	(2.305)	(1.400)	(1.140)	(1.862)	(2.055)	(1.211)	(2.161)	(1.687)	(1.259)	(2.369)	(2.055)
No. reflections	97006	74744	52431	18756	15410	33876	204857	51811	28922	21044	9542	50735	22794	12276	31937
	(9462)	(6907)	(4950)	(1878)	(1500)	(3364)	(20288)	(5206)	(2847)	(2047)	(932)	(4912)	(2306)	(1187)	(3147)
No. atoms	13130	12881	12885	2175	2303	6346	10772	3659	3618	3546	985	1977	3451	907	4260
Protein	12615	12615	12615	2059	2048	5982	8994	3288	3288	3288	827	1644	3288	816	4189
Ligand/ion	2	266	270	70	202	270	603	/	140	232	81	92	90	46	/
Water	513	/	/	45	53	94	1175	371	190	26	77	268	73	45	71
B-factors	47.39	59.91	73.72	60.66	59.78	55.65	17.60	35.16	30.37	61.49	27.59	25.80	46.47	40.19	50.17
Protein	47.60	59.90	73.97	60.78	60.68	55.91	17.17	34.44	30.60	61.78	27.09	24.52	46.55	40.67	50.28
Ligand/ion	55.94	60.36	62.16	57.73	52.81	52.58	11.78	/	20.28	58.26	25.75	17.40	45.34	27.52	/
Water	42.10	/	/	56.78	51.52	47.70	23.83	41.50	33.89	52.75	34.90	36.55	44.33	44.39	43.49
R.m.s. deviations															
Bond lengths (Å)	0.025	0.014	0.011	0.006	0.01	0.013	0.009	0.013	0.018	0.01	0.014	0.012	0.01	0.012	0.017
Bond angles (°)	2.52	2.12	1.26	1.02	1.43	2.05	1.24	1.52	2.20	1.18	1.54	2.03	1.13	1.30	1.59

For each structure one crystal was used.

*Values in parentheses are for highest-resolution shell.

Table containing details of X-ray crystallographical data collection, processing, and refinement including relevant statistics of the maps and models generated in this study.

Reporting Summary

Nature Portfolio wishes to improve the reproducibility of the work that we publish. This form provides structure for consistency and transparency in reporting. For further information on Nature Portfolio policies, see our [Editorial Policies](#) and the [Editorial Policy Checklist](#).

Statistics

For all statistical analyses, confirm that the following items are present in the figure legend, table legend, main text, or Methods section.

n/a Confirmed

- The exact sample size (n) for each experimental group/condition, given as a discrete number and unit of measurement
- A statement on whether measurements were taken from distinct samples or whether the same sample was measured repeatedly
- The statistical test(s) used AND whether they are one- or two-sided
Only common tests should be described solely by name; describe more complex techniques in the Methods section.
- A description of all covariates tested
- A description of any assumptions or corrections, such as tests of normality and adjustment for multiple comparisons
- A full description of the statistical parameters including central tendency (e.g. means) or other basic estimates (e.g. regression coefficient) AND variation (e.g. standard deviation) or associated estimates of uncertainty (e.g. confidence intervals)
- For null hypothesis testing, the test statistic (e.g. F , t , r) with confidence intervals, effect sizes, degrees of freedom and P value noted
Give P values as exact values whenever suitable.
- For Bayesian analysis, information on the choice of priors and Markov chain Monte Carlo settings
- For hierarchical and complex designs, identification of the appropriate level for tests and full reporting of outcomes
- Estimates of effect sizes (e.g. Cohen's d , Pearson's r), indicating how they were calculated

Our web collection on [statistics for biologists](#) contains articles on many of the points above.

Software and code

Policy information about [availability of computer code](#)

Data collection HKL2000 (version 716)

Data analysis CCP4 7.0.078, PyMOL 1.8.4.0, COOT 0.8.9.1, PHENIX 1.17.1-3660, OriginPro 8.0, MAFFT, MMSeq2, FastTree, GraphPad Prism 9, Defense Finder, iTOL v5, Biacore evaluation software

For manuscripts utilizing custom algorithms or software that are central to the research but not yet described in published literature, software must be made available to editors and reviewers. We strongly encourage code deposition in a community repository (e.g. GitHub). See the Nature Portfolio [guidelines for submitting code & software](#) for further information.

Data

Policy information about [availability of data](#)

All manuscripts must include a [data availability statement](#). This statement should provide the following information, where applicable:

- Accession codes, unique identifiers, or web links for publicly available datasets
- A description of any restrictions on data availability
- For clinical datasets or third party data, please ensure that the statement adheres to our [policy](#)

The accession numbers for the coordinate and structure factors reported in this paper are PDB: 8KBB (apo-CmTad1), 8KBC (CmTad1-cA3), 8KBD (CmTad1-cAAG), 8KBE (CbTad1-1'',3'-gcADPR), 8KBF (CbTad1-1'',3'-gcADPR-cA3), 8KBG (CbTad1-2'',3'-cGAMP), 8KBH (CbTad1-2'',3'-cGAMP-cA3), 8KBI (apo-HgmTad2), 8KBJ

(HgmTad2-1'',2'-gcADPR) 8KBK (HgmTad2-1'',2'-gcADPR-cGG), 8KBL (HgmTad2-1''-3'-gcADPR-cGG), 8KBM (HgmTad2-cGG), 8WJC (HgmTad2-3',3'-cGAMP), 8WJD (SptTad2-cGG) and 8WJE (apo-SPO1 Tad2).

Research involving human participants, their data, or biological material

Policy information about studies with [human participants or human data](#). See also policy information about [sex, gender \(identity/presentation\), and sexual orientation](#) and [race, ethnicity and racism](#).

Reporting on sex and gender

Not Applicable.

Reporting on race, ethnicity, or other socially relevant groupings

Not Applicable.

Population characteristics

Not Applicable.

Recruitment

Not Applicable.

Ethics oversight

Not Applicable.

Note that full information on the approval of the study protocol must also be provided in the manuscript.

Field-specific reporting

Please select the one below that is the best fit for your research. If you are not sure, read the appropriate sections before making your selection.

Life sciences

Behavioural & social sciences

Ecological, evolutionary & environmental sciences

For a reference copy of the document with all sections, see nature.com/documents/nr-reporting-summary-flat.pdf

Life sciences study design

All studies must disclose on these points even when the disclosure is negative.

Sample size

No sample size calculation was performed. For in vitro biochemical studies, three independent experiments were widely accepted and used in published paper (such as Nat Chem Biol. 17(4):387-393. doi: 10.1038/s41589-020-00721-2).

Data exclusions

No data were excluded from the analyses.

Replication

The experiments were performed independently for at least three times. All attempts at replication were successful.

Randomization

Randomization is not relevant to the majority of experiments of this study, because protein samples are not required to be allocated into experimental groups in the in vitro activity assays and biochemical studies, and no animals or human research participants are involved in this study. Randomization was used only in structure refinement (Rfree) and it was random.

Blinding

Blinding was not relevant to this study, since no manual counting or scoring was performed to obtain data. And group allocation is not used.

Reporting for specific materials, systems and methods

We require information from authors about some types of materials, experimental systems and methods used in many studies. Here, indicate whether each material, system or method listed is relevant to your study. If you are not sure if a list item applies to your research, read the appropriate section before selecting a response.

Materials & experimental systems

- | | |
|-------------------------------------|--|
| n/a | Involved in the study |
| <input checked="" type="checkbox"/> | <input type="checkbox"/> Antibodies |
| <input checked="" type="checkbox"/> | <input type="checkbox"/> Eukaryotic cell lines |
| <input checked="" type="checkbox"/> | <input type="checkbox"/> Palaeontology and archaeology |
| <input checked="" type="checkbox"/> | <input type="checkbox"/> Animals and other organisms |
| <input checked="" type="checkbox"/> | <input type="checkbox"/> Clinical data |
| <input checked="" type="checkbox"/> | <input type="checkbox"/> Dual use research of concern |
| <input checked="" type="checkbox"/> | <input type="checkbox"/> Plants |

Methods

- | | |
|-------------------------------------|---|
| n/a | Involved in the study |
| <input checked="" type="checkbox"/> | <input type="checkbox"/> ChIP-seq |
| <input checked="" type="checkbox"/> | <input type="checkbox"/> Flow cytometry |
| <input checked="" type="checkbox"/> | <input type="checkbox"/> MRI-based neuroimaging |

Plants

Seed stocks

Not Applicable.

Novel plant genotypes

Not Applicable.

Authentication

Describe any authentication procedures for each seed stock used or novel genotype generated. Describe any experiments used to assess the effect of a mutation and, where applicable, how potential secondary effects (e.g. second site T-DNA insertions, mosaicism, off-target gene editing) were examined.